

Full waveform inversion by model extension

Guillaume Barnier and Ettore Biondi

ABSTRACT

We show that full waveform inversion by model extension (FWIME) combined with a model-space multi-scale approach has the potential to become a robust velocity model-building algorithm that mitigates the cycle-skipping issues inherent to conventional FWI. Its consistent and concise mathematical formulation coupled with an automatized implementation makes it simple to apply and thus more accessible to a broad range of non-expert users. We first apply FWIME to recover a very accurate and high-resolution Marmousi model by starting with a naive initial guess and without the use of low-frequency energy. We dramatically improve the results obtained in our previous report. In a second numerical example, we show that FWIME has the ability to correctly update large areas with substantial kinematic errors and mispositioned sharp interfaces. These conclusive numerical tests improved our understanding of the technique and showed promise as we move towards applying FWIME to field data which requires handling elastic effects and complex overburdens.

INTRODUCTION

Full waveform inversion (FWI) has the potential of inverting all model scales and providing high resolution subsurface images but it is greatly hampered by its sensitivity to the accuracy of the initial model, commonly known as cycle-skipping (Virieux and Operto, 2009). Biondi and Almomin (2014) use an extended model approach to mitigate this issue, but the method, based on a nested-scheme algorithm, heavily relies on the user to tune the many inversion parameters employed in the optimization process.

Following their work, we proposed a modified approach, also relying on an extended Born modeling operator, and showed its potential by successfully inverting cycle-skipped transmission data (Barnier et al., 2018a) and pure reflection data (Barnier and Biondi, 2019). We name this technique full waveform inversion by model extension (FWIME). The main differences in our method is that we do not separate the model parameter into a background (low-wavenumber) and a strictly high-wavenumber perturbation. Moreover, during our inversion process, we aim at completely removing all the energy present in the extended model perturbation and we attach no physical meaning to it. The use of the variable projection method to compute the adequate extended model perturbation allows us to better control the phase alignment of the data residuals (Golub and Pereyra, 1973; Rickett, 2013; Huang and Symes, 2015).

Our ideal research goal is to provide the industry with a P-wave velocity-model building algorithm that is robust (against cycle-skipping issues), mathematically consistent, and implemented in such a way that a broad range of non-expert users may access it and operate it on field data.

As discussed in Barnier et al. (2019), we think the success of waveform inversion at converging towards a useful solution (in an efficient manner) requires an accurate updating of the low-wavenumber components at early stages of the workflow. Biondi and Almomin (2012, 2013) successfully used scale-separation and wavelength-continuation to improve convergence, but their approach remains quite user intensive. We recently proposed to make this process more automatic by incorporating the model-space multi-scale method developed in Barnier et al. (2019) to our FWIME workflow. The entire data bandwidth is simultaneously inverted and the wavenumber content of the updates is controlled by the refinement rate of the spline grid on which the model is parametrized. The benefit of this technique is that all events in the data (including reflections) are used to update the low-wavenumber components (of the model) at early stages.

In this report, we present our recent results obtained on two synthetic examples. First, we invert data generated with the Marmousi model (Martin et al., 2006) starting with a naive linear $v(z)$ initial model and with no available energy below 4 Hz. The recovered model is very accurate, high-resolution, and compares to the model obtained by conducting FWI with unrealistic low frequency energy (starting at 0 Hz).

The model for the second numerical example was designed and kindly provided to us by the Seiscope consortium. It consists of two horizontal layers separated by a sharp and strong velocity-contrast interface and where a large synclinal basin is embedded in the deeper layer. The curvature of the basin is such that it generates very complex waveforms (e.g., triplications) in the reflected wavefields and recorded data (which consist mostly of reflected events). The provided initial model is identical to the true one but does not contain the synclinal feature. This example poses two major challenges. First, it assesses the inversion method’s ability to correctly identify and unravel the “phase” of each events where “different kind of synthetic and observed complex waveforms are tentatively compared”. Secondly, it tests the capacity of the algorithm to correctly update and “move” large areas/geo-bodies presenting strong velocity-contrasts with respect to their surroundings and sharp mispositioned boundaries/interfaces. The ability of our algorithm to correctly handle these two challenges is a necessary (but not sufficient) condition as we move towards applying it to regions with complex overburdens.

For both numerical examples, we present our results following a similar structure. (1) We start by conducting an “ideal” data-space multi-scale FWI workflow by using unrealistic low-frequency energy (as low as 0 Hz). This step serves as an ideal benchmark result to later compare with our FWIME. (2) We then conduct a realistic data-space multi-scale FWI assuming no available low-frequency energy. This step is important to us as we want to ensure that conventional FWI converges to a local minimum (and that there is a need/value to apply our method). (3) We guide the

reader through the initial step of our FWIME workflow which is key to understand the method. We try to give plenty of details so that the reader may gain better insight on how to choose the main parameters of the inversion and their effect on the results. (4) We present our results obtained with our FWIME workflow. We show the recovered models before each spline grid refinement, the convergence curves, the predicted data computed with the various inverted models, we conduct a (wavenumber) spectral analysis of the model updates, and conclude our analysis with an imaging step by computing the migrated images (extended in subsurface reflection angles) at the initial and final stages of FWIME. (5) Finally, we provide a brief summary of each experiment.

THEORY

In our FWIME formulation, we propose to minimize the following objective function defined as

$$\Phi_\epsilon(\mathbf{m}) = \frac{1}{2} \left\| \mathbf{T}_d \left(\mathbf{f}(\mathbf{S}\mathbf{m}) + \tilde{\mathbf{B}}(\mathbf{S}\mathbf{m})\tilde{\mathbf{p}}_{opt}^\epsilon(\mathbf{S}\mathbf{m}) - \mathbf{d}^{obs} \right) \right\|_2^2 + \frac{\epsilon^2}{2} \left\| \mathbf{D}\tilde{\mathbf{p}}_{opt}^\epsilon(\mathbf{S}\mathbf{m}) \right\|_2^2, \quad (1)$$

where \mathbf{m} is the velocity model defined on a (coarse) spline grid, \mathbf{S} is the spline interpolation operator defined in Barnier et al. (2019), \mathbf{f} is the wave-equation operator (acoustic, isotropic), and $\tilde{\mathbf{B}}$ denotes the extended Born modeling operator. Possible extensions include time-lags, subsurface offsets, or shot records (Biondi and Almomin, 2014; Huang and Symes, 2015). In this report, we show applications of FWIME by using time-lag extensions (first numerical example on the Marmosui model) and horizontal subsurface offset extension (second numerical example on the “syncline” Seiscope model). All extended operations (and operators) are denoted by the \sim symbol. \mathbf{d}^{obs} represents the observed data, and \mathbf{T}_d is a self-adjoint data tapering operator (typically employed to mute all refracted energy) whose coefficients are fixed during the entire inversion workflow. The (linear) operator \mathbf{D} is an invertible version of the differential semblance optimization (DSO) operator that enhances the non-physical extended energy of extended images (Symes and Kern, 1994). ϵ is the trade-off parameter between the data-fitting and the regularization terms. The subscript ϵ in Φ_ϵ indicates that ϵ is a fixed parameter throughout the inversion. $\tilde{\mathbf{p}}_{opt}^\epsilon$ is an extended perturbation, defined as the minimizer of the following quadratic objective function $\Phi_{\epsilon,\mathbf{m}}$,

$$\Phi_{\epsilon,\mathbf{m}}(\tilde{\mathbf{p}}) = \frac{1}{2} \left\| \mathbf{T}_d \left(\tilde{\mathbf{B}}(\mathbf{S}\mathbf{m})\tilde{\mathbf{p}} - (\mathbf{d}^{obs} - \mathbf{f}(\mathbf{S}\mathbf{m})) \right) \right\|_2^2 + \frac{\epsilon^2}{2} \left\| \mathbf{D}\tilde{\mathbf{p}} \right\|_2^2. \quad (2)$$

Assuming the Hessian matrix of $\Phi_{\epsilon,\mathbf{m}}$ (equation 2) is positive definite, $\tilde{\mathbf{p}}_{opt}^\epsilon$ is given by

$$\tilde{\mathbf{p}}_{opt}^\epsilon(\mathbf{S}\mathbf{m}) = [\tilde{\mathbf{B}}^*(\mathbf{S}\mathbf{m}) \mathbf{T}_d^2 \tilde{\mathbf{B}}(\mathbf{S}\mathbf{m}) + \epsilon^2 \mathbf{D}^* \mathbf{D}]^{-1} \tilde{\mathbf{B}}^*(\mathbf{S}\mathbf{m}) \mathbf{T}_d^2 (\mathbf{d}^{obs} - \mathbf{f}(\mathbf{S}\mathbf{m})), \quad (3)$$

where $*$ denotes adjoint operators. The minimization of equation 2 is performed using a linear conjugate-gradient algorithm, and is referred to as the variable projection step in FWIME. The data residual component (first term) on the right side of equation 2 is a modified FWI objective function where an additional term $\tilde{\mathbf{B}}(\mathbf{S}\mathbf{m})\tilde{\mathbf{p}}_{opt}^\epsilon(\mathbf{S}\mathbf{m})$ is used to ensure the phase alignment between modeled and observed data. During the optimization process we gradually reduce the contribution of this additional term by adding a regularization term on the right side of equation 1 (which gradually forces the L_2 -norm of $\tilde{\mathbf{p}}_{opt}^\epsilon$ to vanish). It is important to notice that unlike the method proposed in Biondi and Almomin (2014), $\tilde{\mathbf{p}}_{opt}^\epsilon$ may contain all wavenumber components at any stage of the inversion process, and no explicit scale mixing is applied at any step. Hence, $\tilde{\mathbf{p}}_{opt}^\epsilon$ is not defined on the spline grid, but rather on the (finer) finite-difference grid.

Equation 1 is minimized using a gradient-based descent method and its gradient is given by

$$\nabla\Phi_\epsilon(\mathbf{m}) = \mathbf{S}^*\mathbf{M}\left[\mathbf{B}^*(\mathbf{S}\mathbf{m}) + \mathbf{T}^*(\mathbf{S}\mathbf{m})\right]\mathbf{T}_d^2\left(\mathbf{f}(\mathbf{S}\mathbf{m}) + \tilde{\mathbf{B}}(\mathbf{S}\mathbf{m})\tilde{\mathbf{p}}_{opt}^\epsilon(\mathbf{S}\mathbf{m}) - \mathbf{d}^{obs}\right), \quad (4)$$

where \mathbf{B}^* is the adjoint of the non-extended Born modeling operator and \mathbf{T}^* is the adjoint of the tomographic operator (Biondi and Almomin, 2014). The first component of the FWIME gradient in equation 4 (the output of the application of \mathbf{B}^* to the FWIME data residual) will be referred to as the ‘‘Born gradient’’ or ‘‘Born component of the gradient’’ of FWIME. It is computed with the same operator as the one used for conventional FWI gradient but the input (i.e., the data residual) is different. In addition, the second component (stemming from the application of \mathbf{T}^*) updates regions of the model wavenumber spectrum missed by the first one. We refer to it as the ‘‘tomographic gradient’’ or ‘‘tomographic component of the gradient’’ of FWIME. \mathbf{M} is a masking operator that may be used to restrict the gradient from updating certain regions of the model (e.g., the water layer).

The effect of the spline parametrization on the gradient can be understood from equation 4. \mathbf{S}^* (the adjoint of the spline interpolation operator) projects the conventional FWIME gradient onto a (usually coarser) spline grid, thereby enforcing smoothness on the model updates (Barnier et al., 2019). Indeed, the level of smoothness can be adjusted by refining the spline grid over iterations in order to gradually include higher wavenumber updates into our inverted model. In the next two sections, we illustrate these properties with numerical examples that provide more insight on their benefit and impact on the FWIME workflow.

MARMOUSI MODEL

We test our FWIME workflow on the Marmousi model shown in Figure 1a. The model is approximately 17 km wide, and 3.5 km deep. We generate noise-free pressure data

with a two-way acoustic isotropic finite-difference propagator using a grid spacing of 30 m in both directions. We place 140 sources every 120 m, and 567 receivers every 30 m. Sources and receivers are located at a depth of 30 m, and the data are recorded for 8 s. Figure 2 shows two representative shot gathers generated with sources located at $x = 0$ km and $x = 8$ km, with a wavelet containing energy only within the 4-13 Hz frequency range.

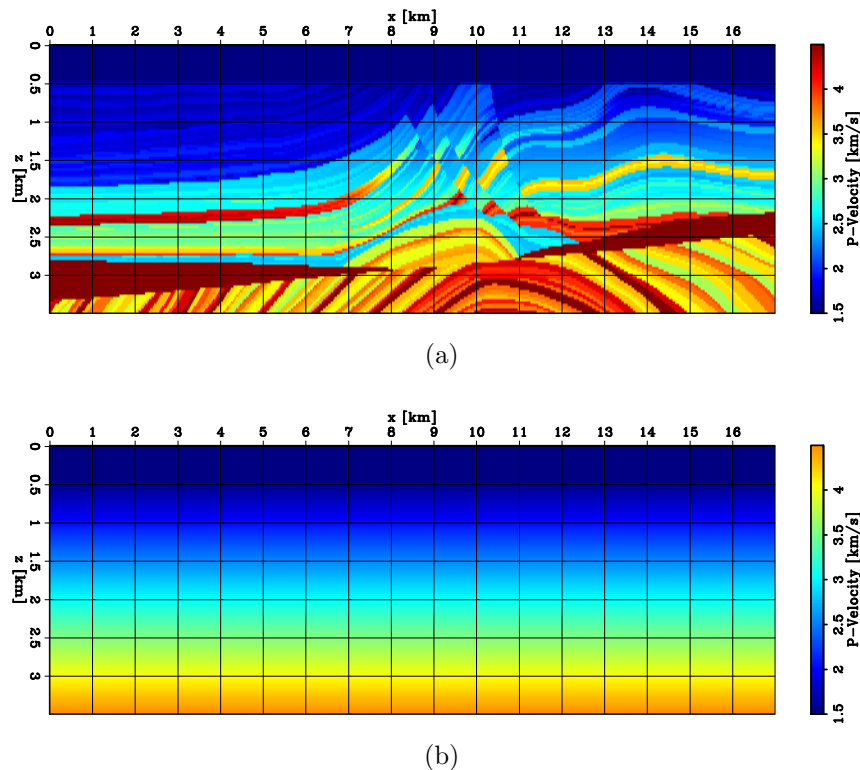


Figure 1: 2D panels of velocity models. (a) True model. (b) Initial velocity model.

Conventional FWI

We conduct two sets of conventional data-space multi-scale FWI. For both tests, we use the same laterally invariant (and linearly increasing with depth) initial velocity model shown in Figure 1b parametrized by $v(z) = a_1 z + b_1$, where $a_1 \approx 0.735 \text{ s}^{-1}$, and $b_1 \approx 1.161 \text{ km/s}$. The velocity profiles of the true and the initial models extracted at various horizontal positions are displayed in Figures 3a-f. In the first FWI test, we use unrealistic ultra-low frequencies to estimate how well the true velocity model could be recovered if these frequencies were available. We use this result as a benchmark to assess the quality of our FWIME method. We invert eight frequency bands shown in Figure 4a. For each band, we conduct 200 iterations of BFGS using the library implemented by Biondi et al. (2019). As expected, the final inverted model is very accurate (Figure 5a). However, when we assume that no energy lower than 4 Hz is available in the recorded data, conventional multi-scale FWI fails to retrieve a useful

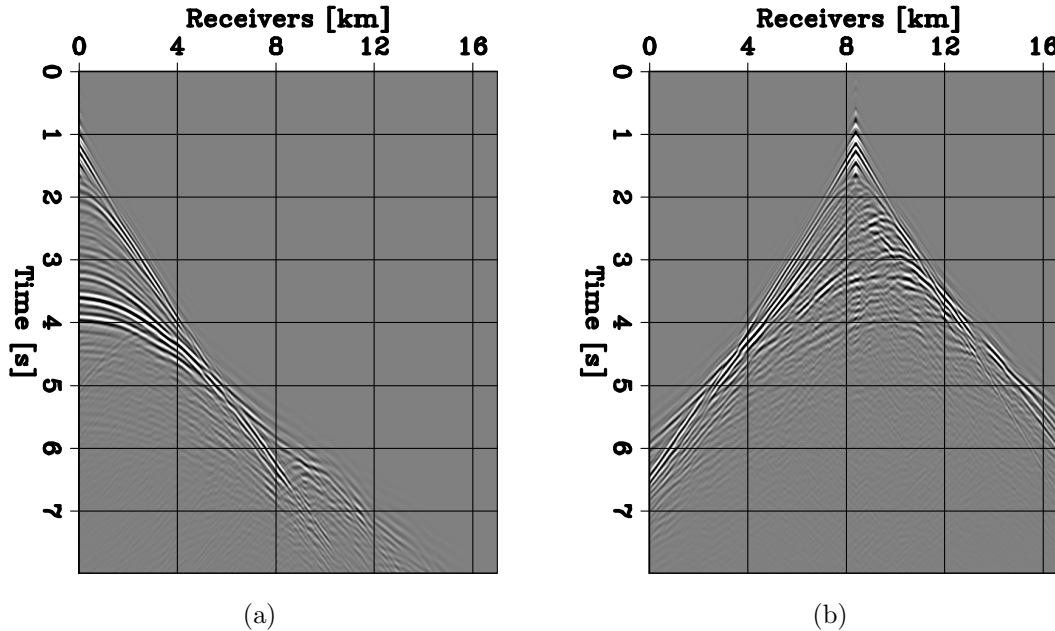


Figure 2: Shot gathers generated with seismic sources containing energy within the 4-13 Hz frequency range. (a) Source located at $x = 0$ km. (b) Source located at $x = 8.2$ km.

solution, especially for depths greater than 1 km (Figure 5b). Even with the presence of some refracted energy, the inaccuracy of the initial model combined with lack of low-frequency energy in the data lead the conventional FWI objective function to converge to a local minimum.

Model-space multi-scale FWIME

We apply our model-space multi-scale FWIME workflow by simultaneously inverting all available data in the 4-13 Hz frequency range, including both refracted and reflected energy (Figure 2). We set the data tapering operator from equation 1 to identity ($\mathbf{T}_d = \mathbf{I}_d$). We use the same linear initial velocity model (parametrized by $v(z) = a_1 z + b_1$) as for the FWI tests (Figure 1b). Throughout this numerical experiment, we use 101 points on the extended axis for the extended optimal perturbation $\tilde{\mathbf{p}}_{opt}^\epsilon$, which provided time-lags ranging from $\tau = -0.8$ s to $\tau = 0.8$ s at a sampling rate of $\Delta\tau = 16$ ms. Each estimation of $\tilde{\mathbf{p}}_{opt}^\epsilon$ (i.e., each variable projection step) is conducted by minimizing objective function shown in equation 2 with 60 iterations of linear conjugate gradient.

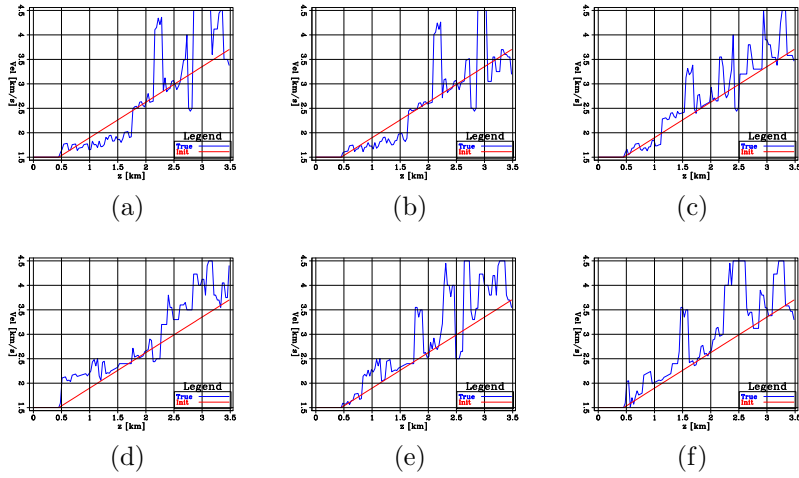


Figure 3: Velocity profiles of the initial (red curve) and true (blue curve) models. (a) $x = 4$ km, (b) $x = 6$ km, (c) $x = 8$ km, (d) $x = 10$ km, (e) $x = 12$ km, and (f) $x = 14$ km.

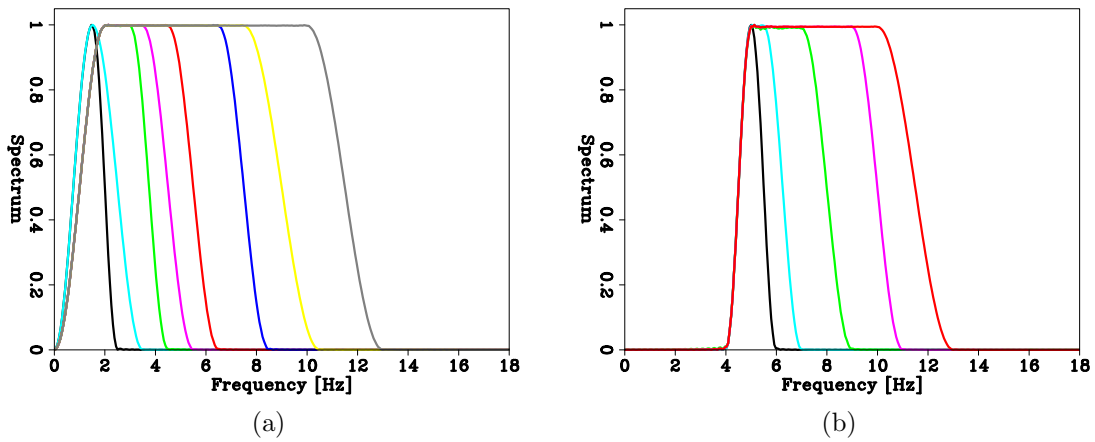


Figure 4: Frequency spectra for the seismic sources used in the numerical experiments. (a) Unrealistic 0-13 Hz scenario. (b) Realistic 4-13 Hz scenario.

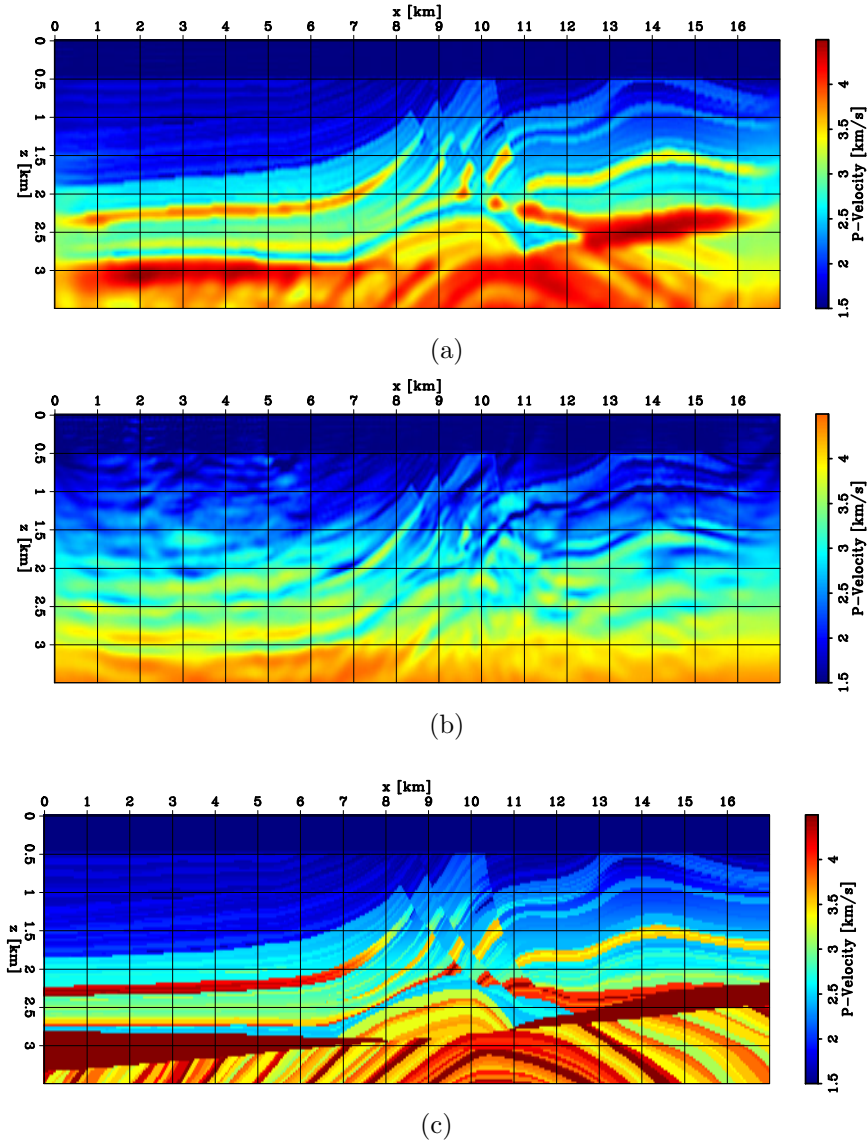


Figure 5: Inverted models with conventional multi-scale FWI. For each frequency band, we conducted 200 iterations of BFGS. (a) Inverted model using the unrealistic 0-13 Hz frequency range. (b) Inverted model using the 4-13 Hz frequency range. (c) True model.

Selection of the trade-off parameter ϵ

The first step of our FWIME workflow consists in selecting the ϵ -value (which remains fixed throughout the entire inversion process). To do so, we compute the initial optimal extended perturbation $\tilde{\mathbf{p}}_{opt}^\epsilon$ (using the initial velocity model) for a wide range of ϵ -values by minimizing objective function 2. As explained in the theoretical section, ϵ serves as a trade-off parameter between the level of data-fitting and the amount of energy that $\tilde{\mathbf{p}}_{opt}^\epsilon$ may contain during the minimization of objective functions 1 and 2. Indeed, during the minimization of objective function 2 (i.e, for a fixed model \mathbf{m}), the value of ϵ does not affect the kinematics of the optimal extended perturbation $\tilde{\mathbf{p}}_{opt}^\epsilon$, but exclusively the amplitude and phase of its energy.

Throughout the minimization of objective function 2, a low ϵ -value will allow the optimal extended perturbation $\tilde{\mathbf{p}}_{opt}^\epsilon$ to contain more energy (both at zero and non-zero time-lags), and will therefore ensure better data-fitting. That is, the first term of objective function 2 should be close to zero. In fact, setting ϵ to zero should lead to a perfect data-fitting (up to numerical precision). To select the length of our extended axis (i.e., the number of points), we conduct a full minimization of objective function 2 while setting ϵ to zero, and we find the minimum length that still ensures that the difference between the initial predicted data and the observed data is perfectly matched (up to numerical precision). That is,

$$\mathbf{T}_d \left(\tilde{\mathbf{B}}(\mathbf{S}\mathbf{m}_{init}) \tilde{\mathbf{p}}_{opt}^{\epsilon=0}(\mathbf{S}\mathbf{m}_{init}) \right) \approx \mathbf{T}_d (\mathbf{d}^{obs} - \mathbf{f}(\mathbf{S}\mathbf{m}_{init})). \quad (5)$$

Satisfying this condition is crucial because it ensures that all the events in the observed data that were not initially predicted (i.e., $\mathbf{d}^{obs} - \mathbf{f}(\mathbf{S}\mathbf{m}_{init})$) are still entirely captured by $\tilde{\mathbf{p}}_{opt}^\epsilon(\mathbf{S}\mathbf{m}_{init})$. If \mathbf{m}_{init} contains large kinematic errors, some of these events will be mapped (i.e., back-projected) into $\tilde{\mathbf{p}}_{opt}^\epsilon(\mathbf{S}\mathbf{m}_{init})$ at large time-lags (far from the zero time-lag axis). Moreover, these events will initially play an important role in FWIME as they provide key kinematic information used when computing the tomographic component of the gradient (Equation 4). The further away from the zero time-lag axis, the more important their contribution will be to the FWIME tomographic gradient (due to the DSO penalty function that enhances energy at larger time-lags with a higher weight). Therefore, by selecting too few points for the extended axis, one may risk to miss these crucial events and not benefit from the kinematic information they bear, which may lead to the FWIME objective function to converge to a local minimum.

On the other hand, increasing the value of ϵ will penalize the presence of energy within $\tilde{\mathbf{p}}_{opt}^\epsilon$ (with a larger penalty applied to the energy located away from the zero time-lag axis), pushing its energy towards the vicinity of the zero time-lag axis and therefore decreasing the level of data-fitting. Moreover, setting ϵ to extremely high values will force the energy of $\tilde{\mathbf{p}}_{opt}^\epsilon$ to first focus towards the zero time-lag axis, and then eventually to completely vanish. As proved in Barnier et al. (2018b), minimiz-

ing our FWIME objective function 1 while setting ϵ to infinity is mathematically equivalent to minimizing the conventional FWI objective function.

The effect of ϵ is clearly noticeable on the initial FWIME data residuals (after minimization of objective function 2 using the initial velocity model) in Figures 6a-d, as well as on the time-lags common image gathers (CIGs) extracted from $\tilde{\mathbf{p}}_{opt}^\epsilon(\mathbf{S}\mathbf{m}_{init})$ at a horizontal position of $x = 10$ km (Figures 7a-d). For $\epsilon = 0$, we can see a very accurate data-fitting (Figure 6a) combined with the presence of strong unfocused energy at larger time-lags (in absolute value terms) in the optimal extended perturbation (Figure 7a). The fact that a great quantity of energy is initially located away from the zero time-lag axis indicates the presence of large kinematic inaccuracies in the initial velocity model. As the value of ϵ increases, we can observe that the data-misfit becomes greater (Figures 6b-d), while the energy within the optimal extended perturbation becomes more focused (Figures 7b and c), and eventually nearly vanishes (Figure 7d).

We are currently investigating ways to automatically select the ϵ -value(s), but it stems from Figures 7a-d (and from multiple tests conducted throughout our research) that picking too high of a value will undermine the benefit of the extension carried by $\tilde{\mathbf{p}}_{opt}^\epsilon$ (all the events bearing information on the kinematic errors disappear from the optimal perturbation and are therefore lost), while selecting too low of a value might not have any meaningful impact on the FWIME workflow. For instance, if $\epsilon = 0$, the data-fitting term of objective function 1 will also be approximately null (or smaller than the noise level), and so will the total FWIME objective function (regardless of how inaccurate the velocity model is). Therefore, the FWIME residuals back-projected to compute the gradient (equation 4) will not be useful as they will just consist of noise.

For this experiment, we chose $\epsilon = 1.5 \times 10^{-5}$ which generated the data-residuals and the CIG shown in Figures 6b and 7b, respectively. We tried conducting our FWIME workflow with various values of ϵ and obtained similar results at least for ϵ ranging from $\epsilon_1 = 1.1 \times 10^{-5}$ to $\epsilon_2 = 5.5 \times 10^{-5}$ (we did not try outside of this range due to a lack of time). However, more tests need to be conducted to evaluate the robustness of our method with respect to this key parameter. For the optimal extended perturbation, we use a total 101 points along the extended axis (time-lags ranging from $\tau = -0.8$ to $\tau = 0.8$ s), which was sufficient to satisfy condition 5.

Initial search direction

To illustrate the effect of the trade-off parameter ϵ on the first FWIME gradient, we compute the initial FWIME search directions for the same range of ϵ -values as the ones used in the previous step. In practice, we would not need to do compute the search directions for all ϵ -values. Figures 8a-c show the initial FWIME search directions on the finite-difference (finer) grid, and Figure 8d shows the ideal search direction.

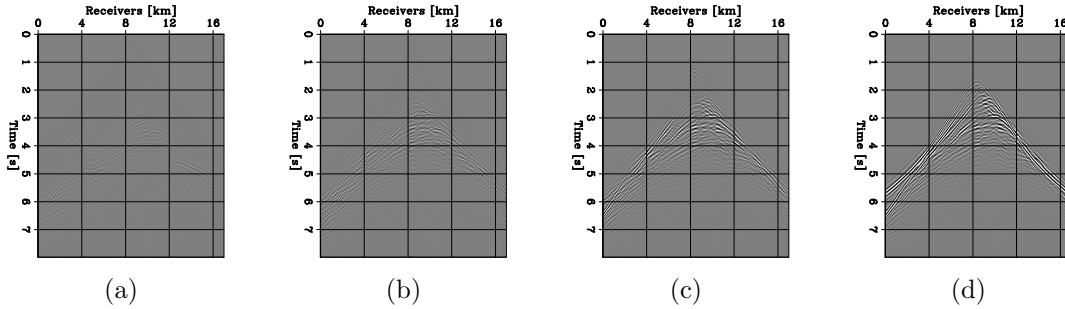


Figure 6: FWIME data residuals after minimization of objective function 2 for various ϵ -values and for a shot located at $x = 8.2$ km. (a) $\epsilon = 0.0$, (b) $\epsilon = 1.5 \times 10^{-5}$, (c) $\epsilon = 8.0 \times 10^{-5}$, and (d) $\epsilon = 2.5 \times 10^{-4}$.

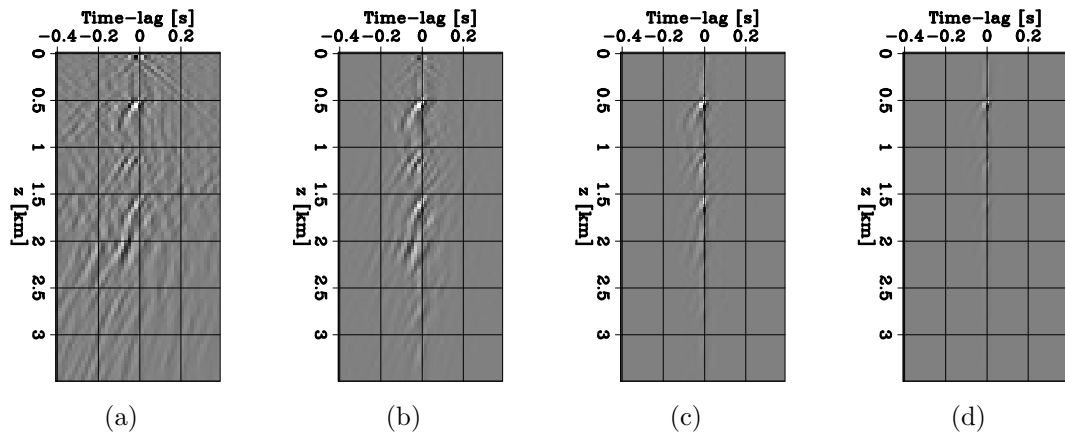


Figure 7: CIG extracted from $\tilde{\mathbf{p}}_{opt}^\epsilon(\mathbf{S}\mathbf{m}_{init})$ at $x = 10$ km after minimization of objective function 2 for various ϵ -values. (a) $\epsilon = 0.0$, (b) $\epsilon = 1.5 \times 10^{-5}$, (c) $\epsilon = 8.0 \times 10^{-5}$, and (d) $\epsilon = 2.5 \times 10^{-4}$.

Our initial (coarse) spline grid is chosen without any prior knowledge of the sub-surface geometry other than the water-bottom depth. We selected a sampling of 200 m in the z -direction, and 1 km in the x -direction. The sampling in the absorbing boundaries is 1 km in both directions and is kept constant for all spline grids throughout this experiment. Figures 9a-c show the analogous FWIME first search directions after projection onto the first spline grid. By comparing the first search direction for our selected ϵ -value (Figure 9a) to the true search direction after projection onto the first spline grid (Figure 9d), we can see the importance of using a spline parametrization in order to initially capture the correct low-wavenumber components of the true model.

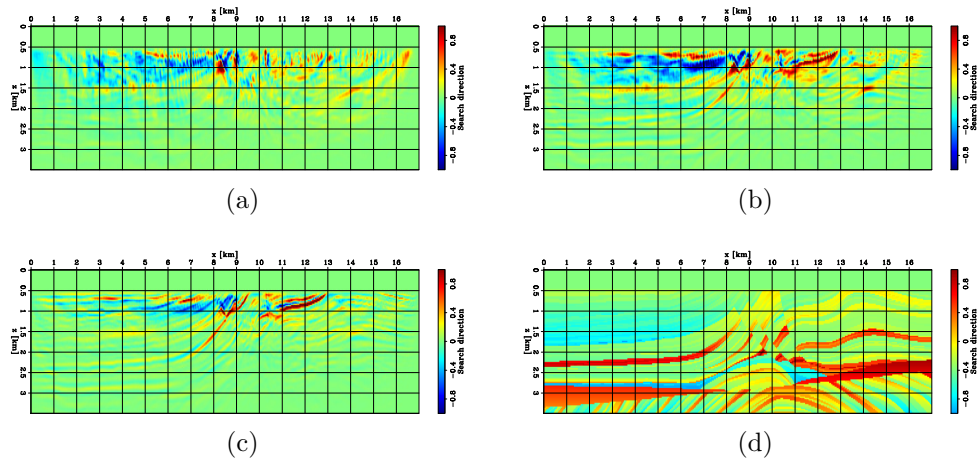


Figure 8: Search directions computed for various ϵ -values. (a) $\epsilon = 1.5 \times 10^{-5}$, (b) $\epsilon = 8.0 \times 10^{-5}$, (c) $\epsilon = 2.5 \times 10^{-4}$, and (d) ideal search direction.

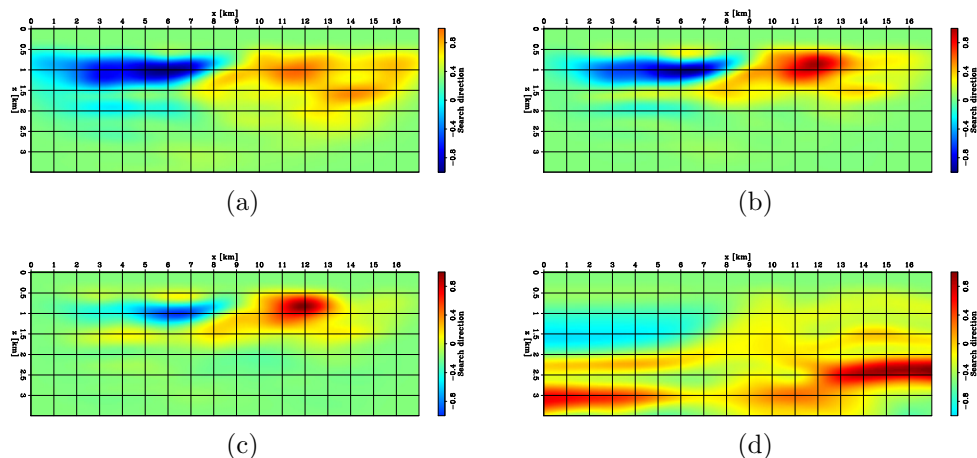


Figure 9: Search directions after projection onto the first spline grid, computed for various ϵ -values. (a) $\epsilon = 1.5 \times 10^{-5}$, (b) $\epsilon = 8.0 \times 10^{-5}$, (c) $\epsilon = 2.5 \times 10^{-4}$, and (d) ideal search direction.

Inversion results

We conduct our model-space multi-scale FWIME workflow using a sequence of four different spline grids, and keeping the same ϵ -value throughout the entire process ($\epsilon = 1.5 \times 10^{-5}$). Each spline grid refinement is triggered when the stepper is unable to find a step length that decreases the FWIME objective function 1. The spacing in the second and third spline grids are obtained by halving the spacing from the previous ones. The fourth (and final) spline grid has the same spacing as the finite-difference grid. As explained in Barnier et al. (2019), the inverted model on a given grid is used as the initial model for the following grid.

Figures 10a-d show the sequence of inverted models throughout our optimization scheme at the end of each grid. The final inverted model (Figure 10e) is close to the optimal solution (Figure 10f). Figures 11a-f show the initial, true, and inverted velocity profiles extracted at various horizontal positions. By comparing it to the FWI inverted model obtained using unrealistic low-frequency energy (Figure 12a) we can clearly see that FWIME workflow managed to converge to an accurate and high-resolution model by recovering both low- and high-wavenumber features using only energy within the 4-13 Hz frequency range. Indeed, it also outperforms the model obtained with the conventional FWI using the more realistic 4-13 Hz frequency range (Figure 12b).

Inversion strategy for a production workflow

For this experiment, we conducted our FWIME workflow for each spline grid until completion (by letting the solver stop by itself) solely in order to show its potential in recovering a high-resolution model as accurate as conventional FWI using unrealistic ultra-low frequencies. To be clear, in this experiment we wanted to assess whether FWIME could converge to the true solution (in an academic context) without the need to modify or tune any parameter along the process. This is the first step towards making FWIME easily accessible to a wider range of users and geophysicists that may not be experts in that particular field. However, we acknowledge that this is not the most efficient strategy in terms of computational costs for multiple reasons. First, using a single ϵ -value for the entire workflow might not be the optimal solution and we are currently investigating the use of the discrepancy principle approach proposed by Fu and Symes (2017). Moreover, in a production workflow (and as we further improve the efficiency of our technique), we would utilize FWIME only to produce an “accurate enough” initial model for FWI to converge towards a useful solution.

In order to determine when the FWIME inverted model is “accurate enough”, one may carefully examine $\tilde{\mathbf{p}}_{opt}^\epsilon$ after each FWIME iteration. As explained in Barnier and Biondi (2019), even though computing $\tilde{\mathbf{p}}_{opt}^\epsilon$ (i.e., the variable projection step) is quite computationally costly, it is however a very accurate and useful quality check (QC) tool. For instance, one could examine the quantity of energy spread away from the zero time-lag axis in the CIGs of $\tilde{\mathbf{p}}_{opt}^\epsilon$ (the less energy, the more accurate the

model). Figure 13 shows the evolution of two CIGs extracted from $\tilde{\mathbf{p}}_{opt}^\epsilon$ (at $x = 3$ km on the top row and $x = 13$ km on the bottom row) at four key stages of our inversion process. Column one was computed at the initial step, while columns two, three and four were computed at the end of spline grids 1, 2, and 3. As expected, the initial model is quite inaccurate and we can see a great amount of unfocused energy (first column). As the inversion advances, it progressively focuses the energy towards the zero time-lag axis, and eventually forces it to completely vanish (this can also be observed by examining the zero time-lag cross-sections of $\tilde{\mathbf{p}}_{opt}^\epsilon$ in Figures 14a-e). We are currently considering automatic ways to quantify this process in order to make it feasible for 3D field data applications (where one could not realistically examine all the CIGs in the inverted volume). One of our current goals is to find a metric (with the help of $\tilde{\mathbf{p}}_{opt}^\epsilon$) that enables us to assess whether a FWIME inverted model is accurate enough for conventional FWI.

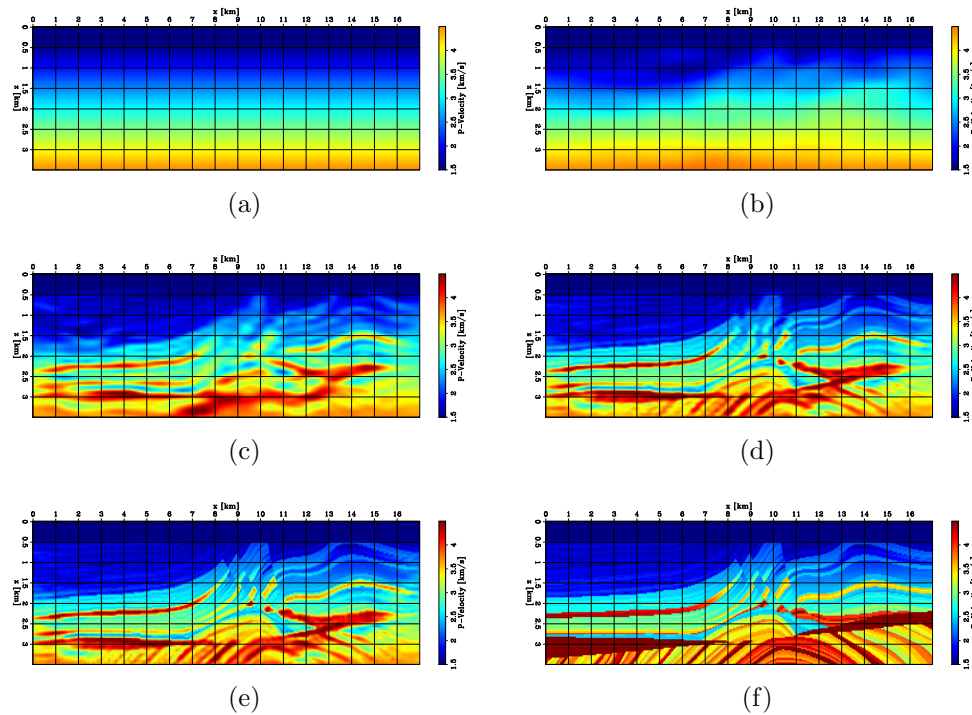


Figure 10: Inverted models at different stages of the model-space multi-scale FWIME workflow using energy within the 4-13 Hz frequency range and $\epsilon = 1.5 \times 10^{-5}$. (a) Initial model. (b) Inverted model after the first spline grid. (c) Inverted model after the second spline grid. (d) Inverted model after the third spline grid. (e) Inverted model after the fourth (finite-difference) grid. (f) True model.

Objective function analysis

Figure 15a shows the value of the scaled FWIME objective functions (equation 1) as a function of iterations throughout the four different stages (four spline grids) of our inversion process. The blue curve corresponds to the total objective function,

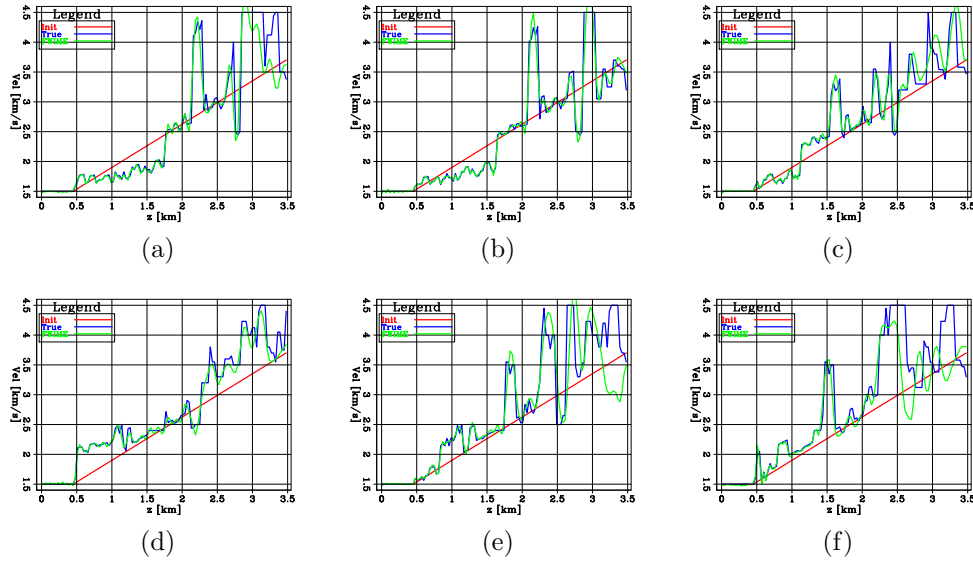
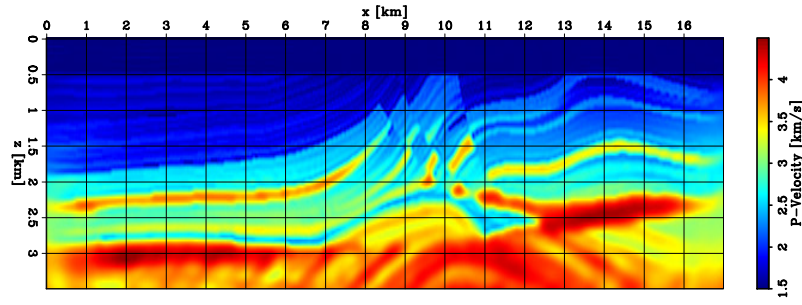


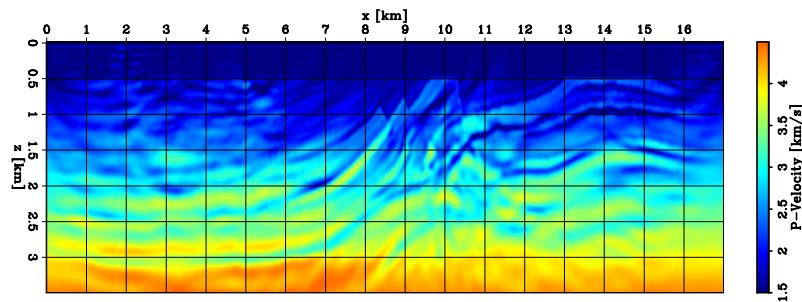
Figure 11: Velocity profiles of the initial (red curve), FWIME (green curve), and true (blue curve) models. (a) $x = 4$ km, (b) $x = 6$ km, (c) $x = 8$ km, (d) $x = 10$ km, and (e) $x = 12$ km. (f) $x = 14$ km.

the red curve corresponds to the data-fitting term, and the pink curve displays the regularization term. We conducted a total of 242 iterations, 24 for spline 1, 64 for spline 2, 104 for spline 3, and 50 for spline 4. The three major changes in convexity occurring at iterations #24, #88, and #192 indicate a spline grid refinement. Figure 15b displays the scaled total FWIME objective function (blue curve) along with the value of the conventional FWI objective function evaluated at each inverted model during the FWIME sequence (red curve). Note that this curve is not the result of an inversion process, but simply an evaluation of the conventional FWI objective function at each FWIME inverted model. This curve is not monotonically decreasing which indicates that the FWIME scheme managed to modify the conventional FWI objective function and has mitigated the presence of local minima inherent to the method. Moreover, we can see that both the FWIME and FWI curves eventually converge to zero (up to numerical precision) which means that FWIME has finally managed to find an inverted model \mathbf{m}_{inv} that matches all observed data without the need of the additional data term stemming from extended perturbation $\tilde{\mathbf{p}}_{opt}^e$. That is,

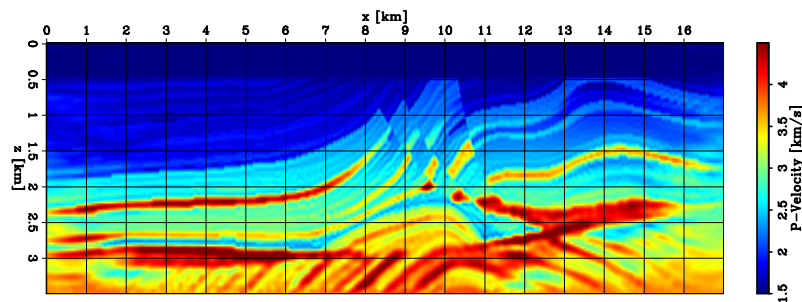
- $\mathbf{f}(\mathbf{m}_{inv}) = \mathbf{d}^{obs}$, and
- $\tilde{\mathbf{p}}_{opt}^e(\mathbf{m}_{inv}) = \mathbf{0}$.



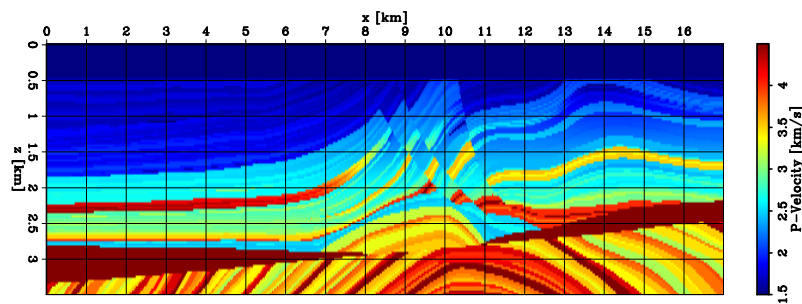
(a)



(b)



(c)



(d)

Figure 12: Summary of the inverted models for this numerical example. (a) Conventional multi-scale FWI using an unrealistic 0-13 Hz energy bandwidth. (b) Conventional multi-scale FWI realistic 4-13 Hz energy bandwidth. (c) FWIME inverted model. (d) True model.

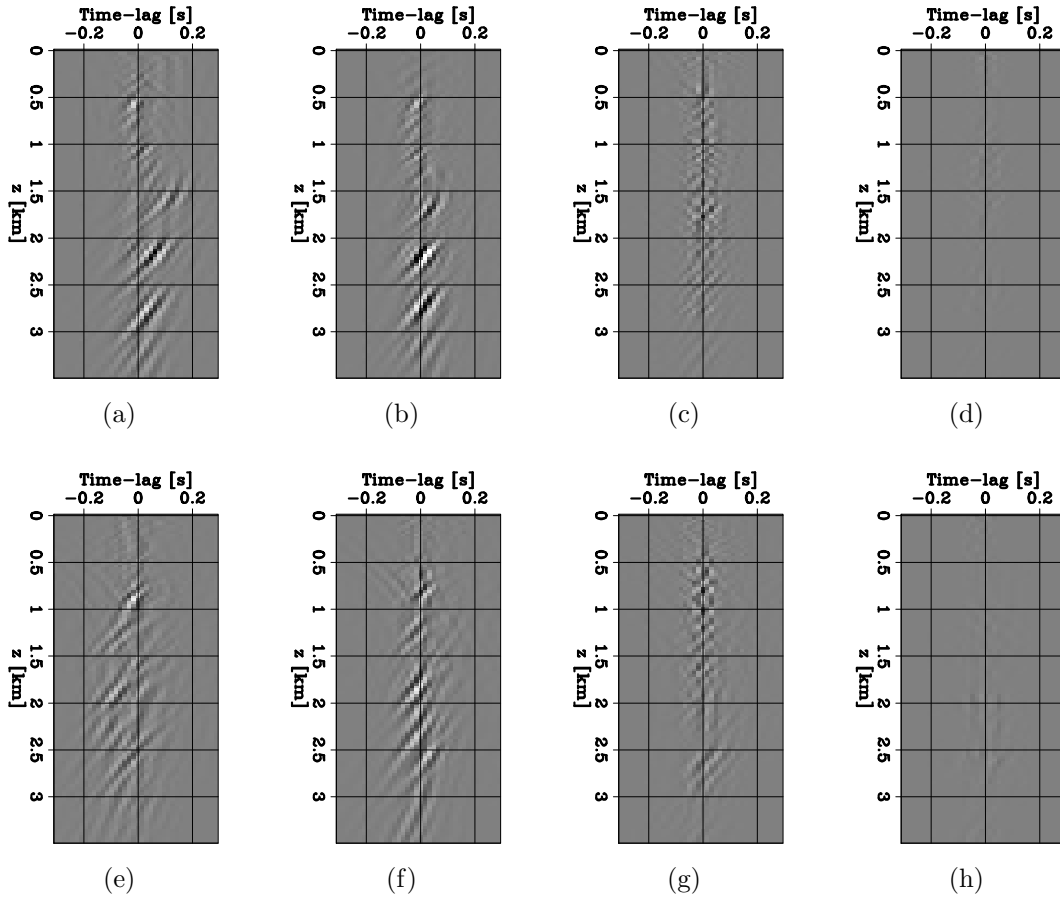


Figure 13: CIGs extracted from $\tilde{\mathbf{p}}_{opt}^\epsilon$ at four stages of the FWIME workflow. CIGs on the top row were extracted at $x = 3$ km, and CIGs from the bottom row were extracted at $x = 13$ km. First column is computed with the initial model, second column after spline 1, third column after spline 2, and fourth column after spline 3. All figures are plotted with the same color scale.

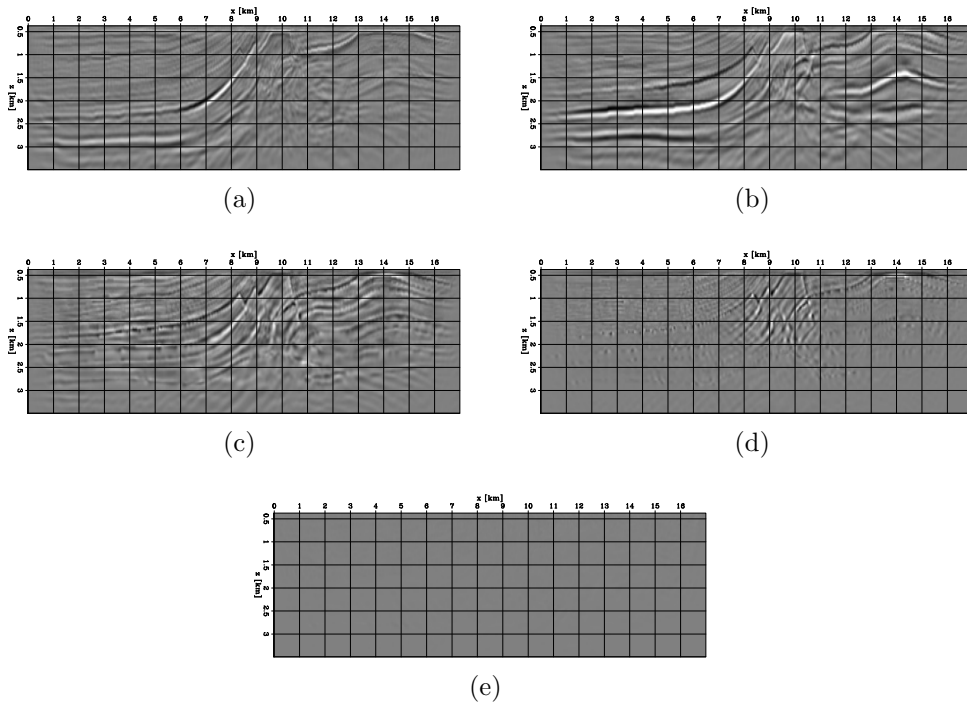


Figure 14: Zero time-lag sections of optimal perturbation $\tilde{\mathbf{p}}_{opt}^\epsilon$ computed at five different stages of the FWIME workflow. (a) Initial. (b) After spline 1. (c) After spline 2. (c) After spline 3 (d) After spline 4 (finite-difference grid).

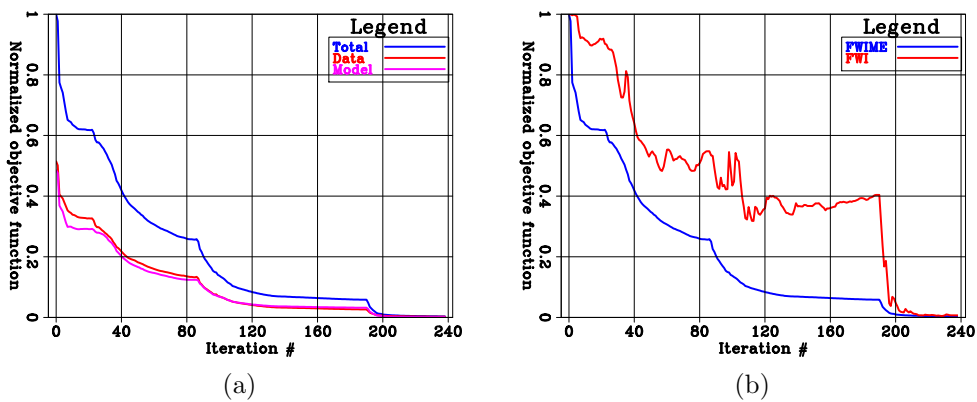


Figure 15: (a) FWIME objective functions from equation 1: total FWIME objective function (blue curve), data-fitting term (red curve), and regularization term (pink curve). (b) Total FWIME objective function (blue curve), and “FWI” objective function evaluated at each FWIME inverted model (red curve).

Data-space analysis

Figure 16 shows the observed data (left column), predicted data (middle column), and data-difference (right column) at the end of each spline grid sequence (each row corresponds to a spline grid sequence), for a source located at a horizontal position of approximately $x = 1$ km. The inversion workflow begins by allowing exclusively low-wavenumber updates into the model (due to the coarse spline grid parametrization), which enforces a better matching of the observed data at larger offsets (second row of Figure 16). Eventually, as we refine the spline grid and allow for higher-wavenumber updates, reflections are progressively matched and the data-residuals vanish (third and fourth rows in Figure 16).

Spectral analysis

Figures 17a-d show the wavenumber spectra of the various model updates (i.e., the amplitude spectrum of the 2D spatial Fourier transform of the difference between the inverted and initial models) obtained after completion of the three different workflows described in this example (unrealistic FWI 0-13 Hz, realistic FWI 4-13 Hz, and FWIME 4-13 Hz). Figure 17a corresponds to the FWI workflow using the unrealistic 0-13 Hz frequency range and Figure 17c corresponds to the FWIME inverted model. As expected, they show great similarity with the “ideal” update (i.e., the difference between the true and the initial models) displayed in Figure 17d. This illustrates the success of the model-space multi-scale FWIME approach at recovering the low-wavenumber components of the true model without the need for low-frequency energy. Figure 17b displays the model-update amplitude spectrum of the FWI inverted model using the 4-13 Hz bandwidth, which clearly fails to capture these crucial low-wavenumber features initially missing. Furthermore, Figure 18a shows the spectrum of the FWIME model update after the first spline grid. We can observe that the initial “coarse” spline grid parametrization (spline 1) only allows low-wavenumber updates to be added to the inverted model (at first). Finally, the higher wavenumber updates are gradually added during the FWIME workflow (Figure 18b).

Imaging

We conduct an imaging QC step in order to assess the quality of our inverted velocity model. Figures 17a and b show the zero-offset sections of the initial and final migrated images, respectively. By comparing them to the true model (Figure 17c), we can clearly see an improvement in the image, especially in the vicinity of the reservoir (red box) where none of the features were initially visible. This observation is also confirmed by examining the subsurface angle domain common image gathers (ADCIG) shown in Figure 20 extracted at four horizontal positions ranging between $x = 9$ km and $x = 12$ km. The top row of Figure 20 shows the ADCIGs computed with the initial velocity model and the bottom row ADCIGs are computed with the

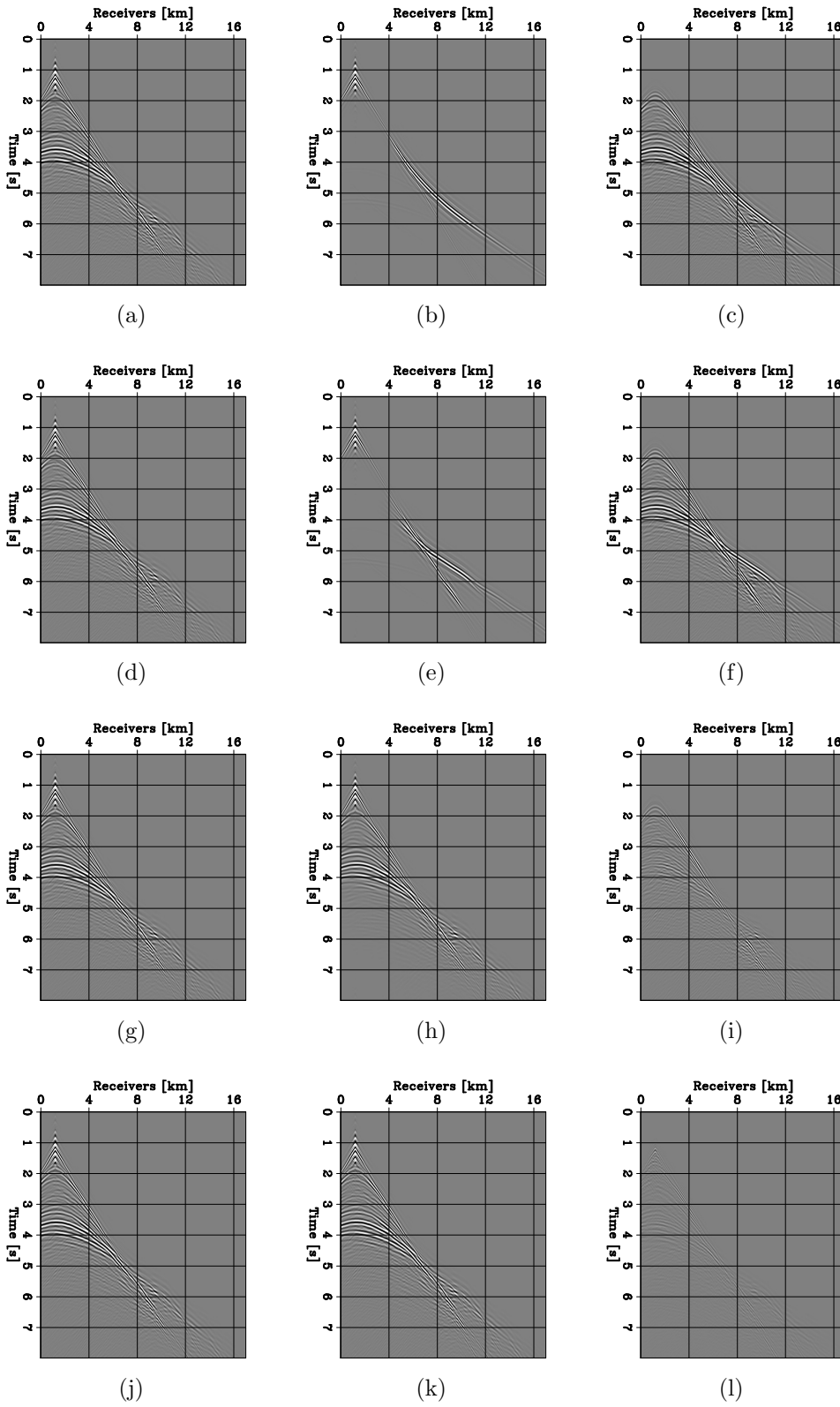


Figure 16: Observed data (left column), predicted data (middle column), and data residual (right column) for a source located at approximately $x = 1$ km. Initial (first row), spline 1 (second row), spline 3 (third row), spline 4 (fourth row).

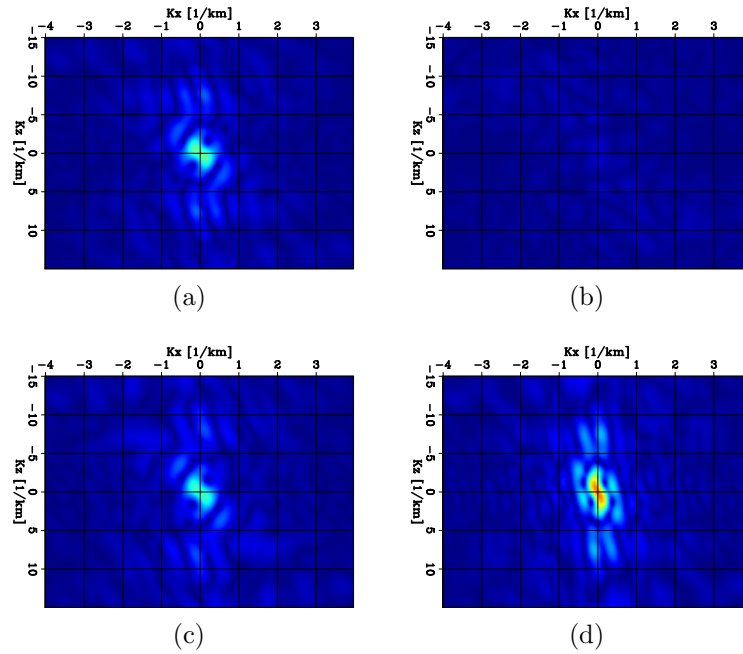


Figure 17: Amplitude Spectra of inverted model updates obtained after the FWI and FWIME workflows. (a) FWI with unrealistic 0-13 Hz frequency band. (b) FWI with realistic 4-13 Hz frequency range. (c) FWIME using 4-13 Hz frequency range. (d) Ideal update (difference between true and initial models).

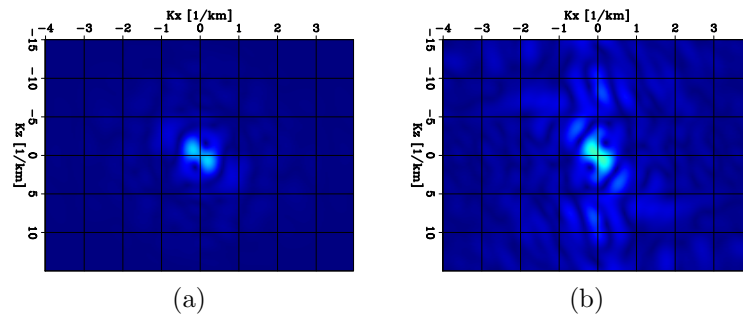


Figure 18: Amplitude Spectra of FWIME inverted model updates. (a) FWIME model update after spline 1. (b) Final FWIME model update.

final inverted model. As expected, the final velocity is able to image the different interfaces at the reservoir level.

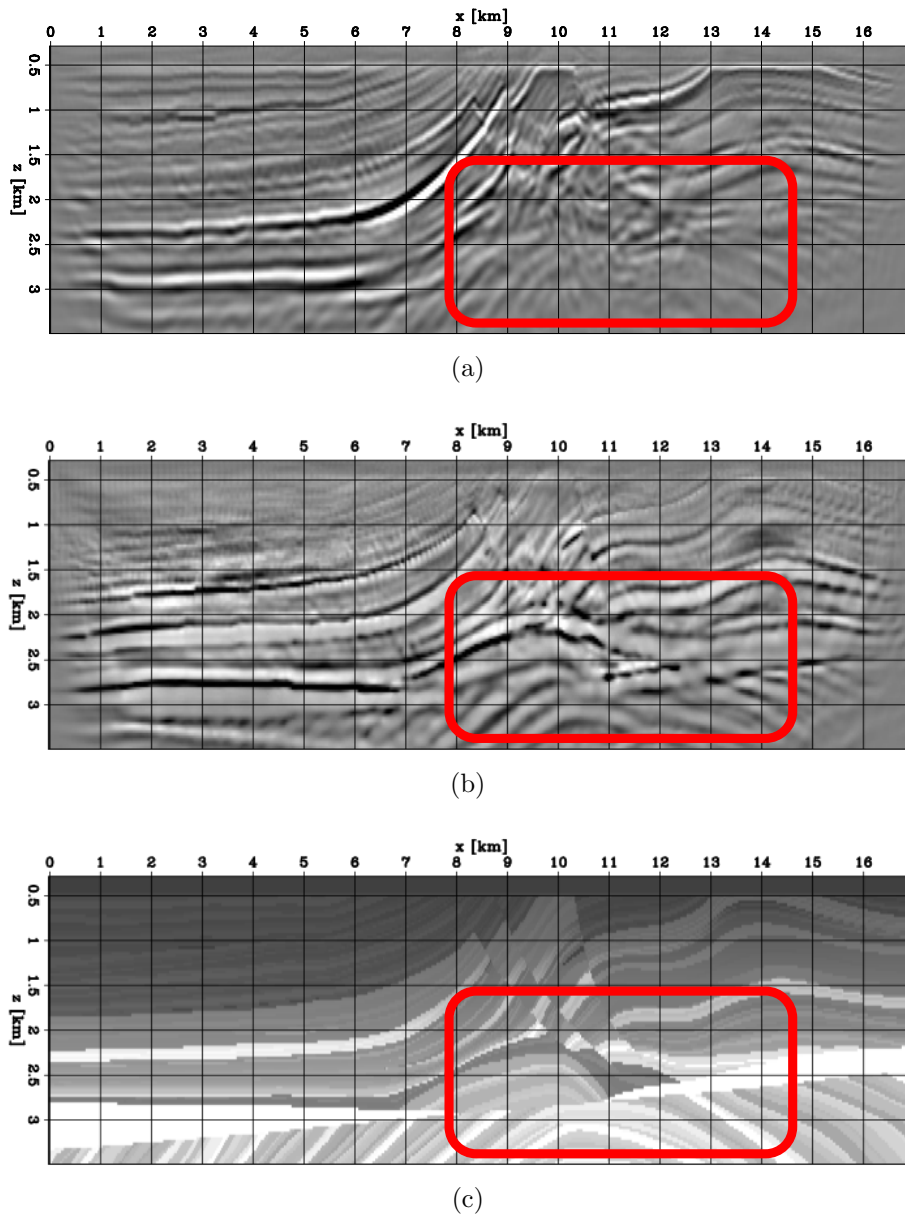


Figure 19: (a) Migrated image with the initial velocity model. (b) Migrated image with the FWIME inverted model. (c) True model.

Summary of the Marmousi example

By conducting this numerical experiment on the well-known benchmark Marmousi model, our goals were twofold: (1) Develop a robust velocity model-building algorithm that mitigates the need for an accurate initial guess and/or low-frequency data, and

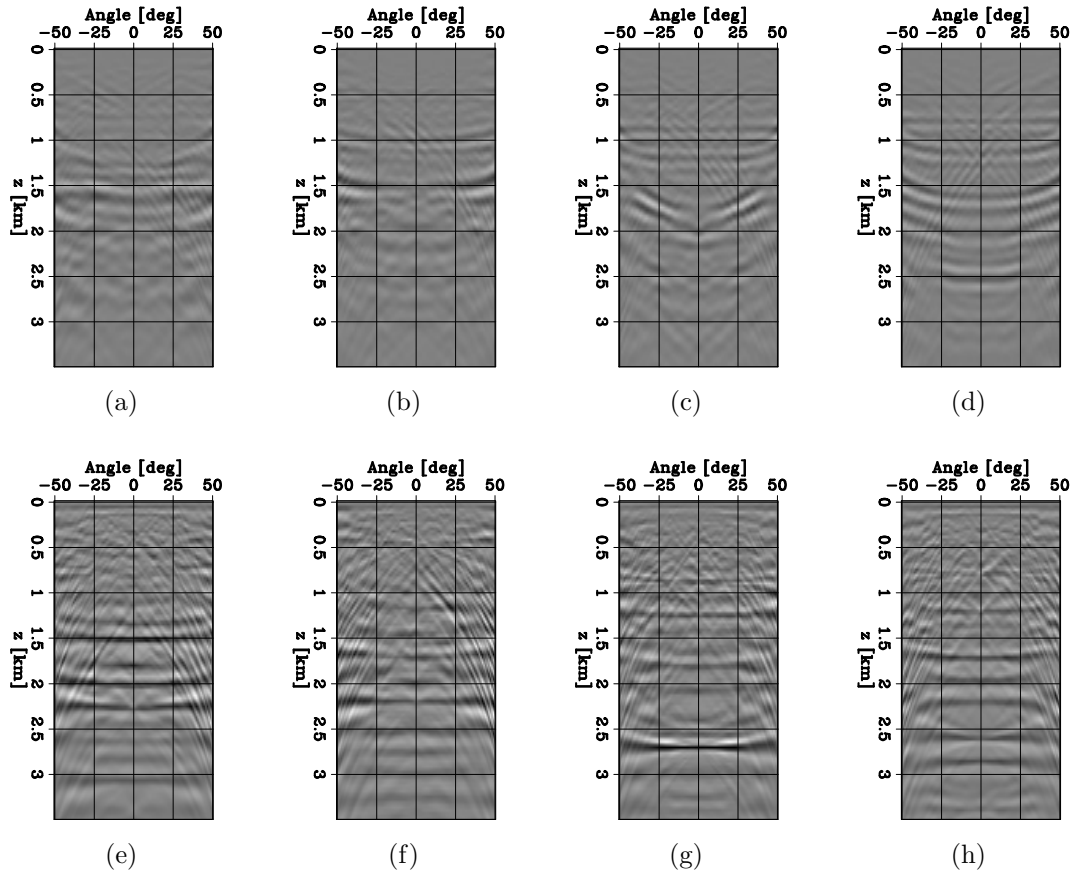


Figure 20: Angle domain common image gathers (ADCIGs) computed with the initial model (top row) and the FWIME inverted model. First column is for $x = 9$ km, second column is for $x = 10$ km, third column is for $x = 11$ km, and fourth column is for $x = 12$ km.

(2) build a process accessible to a broader range of non-expert users. To that end, we managed to successfully apply our FWIME workflow and invert modeled data containing no energy outside of the 4 – 13 Hz frequency range by using an initial model with laterally invariant and linearly increasing velocity values. We recovered a very accurate and high-resolution solution that matched the observed data close to numerical precision. Moreover, even though its efficiency can (and must be) improved for field data applications, our workflow required a minimum amount of user-input during the process (e.g., no user-intensive nested-scheme approach and no need to adjust the trade-off parameter ϵ throughout the entire process).

We wish to stress the fact that our strategy adopted for this benchmark test was likely not the most computationally efficient one. We approached this test as an experiment to further improve our understanding of the method and the calibration of the different parameters. First, we were extremely conservative and cautious when choosing the parameter values such as the length of the extended axis or the number of iterations conducted for each variable projection step. We wanted to avoid taking any potentially risky shortcuts that could have affected the outcome of our result, and therefore our fundamental conclusions on the potential of our technique. Second, we purposely maintained a constant ϵ -value throughout the workflow (to show its ability to be conducted automatically) which has been shown (and confirmed by tests we conducted but not shown in this report) to be sub-optimal. In fact, as we mentioned earlier in the report, we believe including the discrepancy-principle in our approach may dramatically improve the convergence rate of FWIME. Thirdly, the FWIME workflow would never need to be conducted until completion in a production environment. It would be used to deliver an accurate enough starting point for conventional FWI. Finally, this first successful application of FWIME on a realistic scenario will serve as a reference result as we further work on improving the efficiency of our technique.

SYNCLINE MODEL

We apply our FWIME workflow on a synthetic example designed and proposed by the Seiscope consortium in Grenoble, France. The true velocity model is shown in Figure 21a. Figure 22 (blue curve) shows its velocity profile extracted at $x = 4$ km and $x = 6$ km. The model is approximately 12 km wide, and 3.5 km deep, and it is composed of two horizontal layers with a low-velocity synclinal inclusion (basin) embedded in the second (deeper) layer. The initial velocity is shown in Figure 21b and Figure 22 (red curve), and is identical to the true model but does not contain the synclinal basin. The velocity value is $v_s = 2.8$ km/s in the shallow layer, and $v_d = 4.0$ km/s in the deeper layer. The difference between the two velocity models is shown in Figure 21c.

We generate noise-free seismic data using an acoustic, isotropic, constant-density modeling operator. For our finite-difference scheme, we use a grid spacing of 50 m in both directions and a band-passed Ricker wavelet containing energy only within the

1.5-6.5 Hz frequency range (Figure 23). We place 48 shots spaced every 250 m and 255 receivers every 50 m. All acquisition devices are placed at a constant depth of 50 m. Figures 24a and b show two representative shot gathers for sources located at $x = 0.3$ km and $x = 6.3$ km containing energy only within the 1.5-6.5 Hz frequency range.

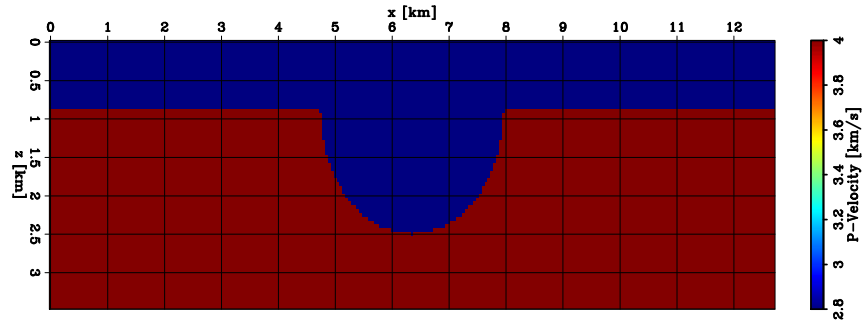
We first conduct a conventional data-space multi-scale FWI workflow and show its inability to retrieve the correct solution, even with the presence of very low frequency energy in the recorded data. We then successfully apply our model-space multi-scale FWIME approach and manage to recover a very accurate model.

Goals of this experiment

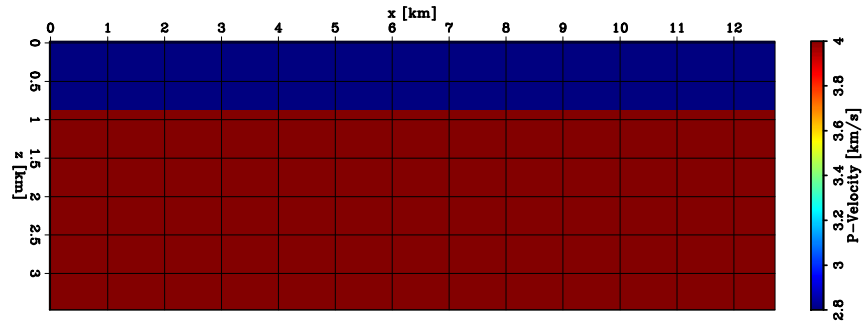
This synthetic problem was designed and developed by a team of researchers led by Weiguang He at the Seiscope consortium, and kindly shared to the Stanford Exploration Project (SEP) group by Dr. Virieux during his visit in May 2019 at Stanford University. The goal of their experiment was to test the robustness of various data-driven waveform inversion methods against the “ill-posedness coming from wrong association of predicted and observed waveforms”. The authors further explain that “this ill-posedness is related to phase identification where different kind of synthetic and observed waveforms are tentatively compared, which could be quite frequent when the current model estimate predicts more or less waveforms than the velocity model corresponding to the observed waveforms”.

In order to generate this type of scenario with a simple numerical experiment, the authors embed a synclinal basin into the deeper layer of a horizontal two-layer model (as detailed in the previous section). The basin curvature is such that the reflected events from the bottom of the basin generate wavefield triplications in the recorded data. Indeed, these events overlap with the reflections from the shallow interface between the two layers. The complexity of the recorded waveforms can be observed in the shot gathers displayed in Figures 24a and b. Moreover, this numerical experiment poses another difficult challenge because its initial model contains a vast region (relative to the dimensions of the area of interest) with mispositioned sharp boundaries and incorrect strong velocity-contrasts with its surroundings.

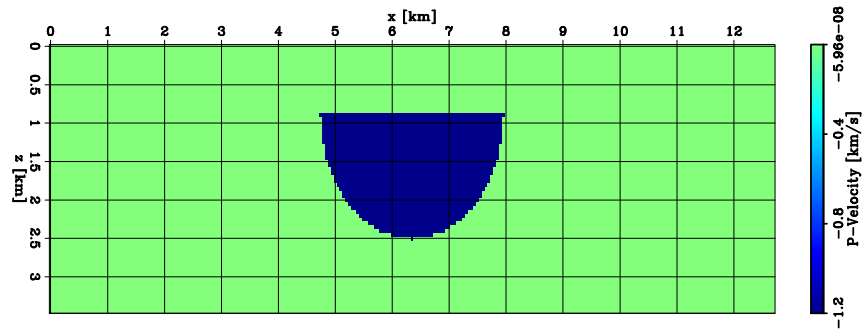
Both difficulties (phase identification and large areas of kinematic errors coupled with mispositioned sharp interfaces) provide a similar (though simpler) scenario to the one encountered when exploring in regions with the presence of complex overburdens (e.g., salt bodies). This is due to the complicated waveforms generated and recorded at the surface (e.g., prismatic reflections from rugose top-salt interface) as well as the difficulty to accurately delineate these complex overburdens. Therefore, testing FWIME on such an example allowed us to gain better insight on its potential ability to perform well in these types of scenarios.



(a)



(b)



(c)

Figure 21: 2D panels of velocity models. Both shallow and deeper layers have a homogeneous velocity value of $v_s = 2.8$ km/s and $v_d = 4.0$ km/s, respectively. (a) True model. (b) Initial velocity model. (c) Model difference.

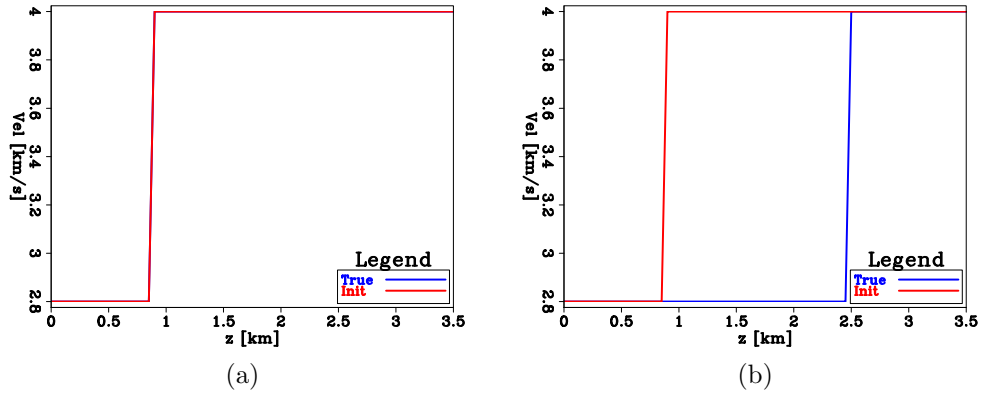


Figure 22: 1D profiles of velocity models. The blue curve corresponds to the true model and the red curve corresponds to the initial model. (a) Velocity profiles extracted at $x = 4$ km. (b) Velocity profiles extracted at $x = 6$ km.

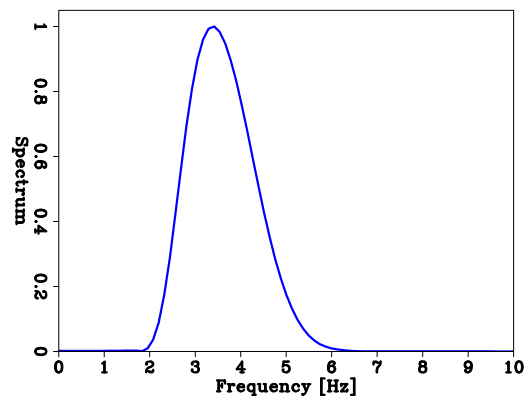


Figure 23: Amplitude spectrum for the seismic source used for both FWI and FWIME workflows in this numerical experiment.

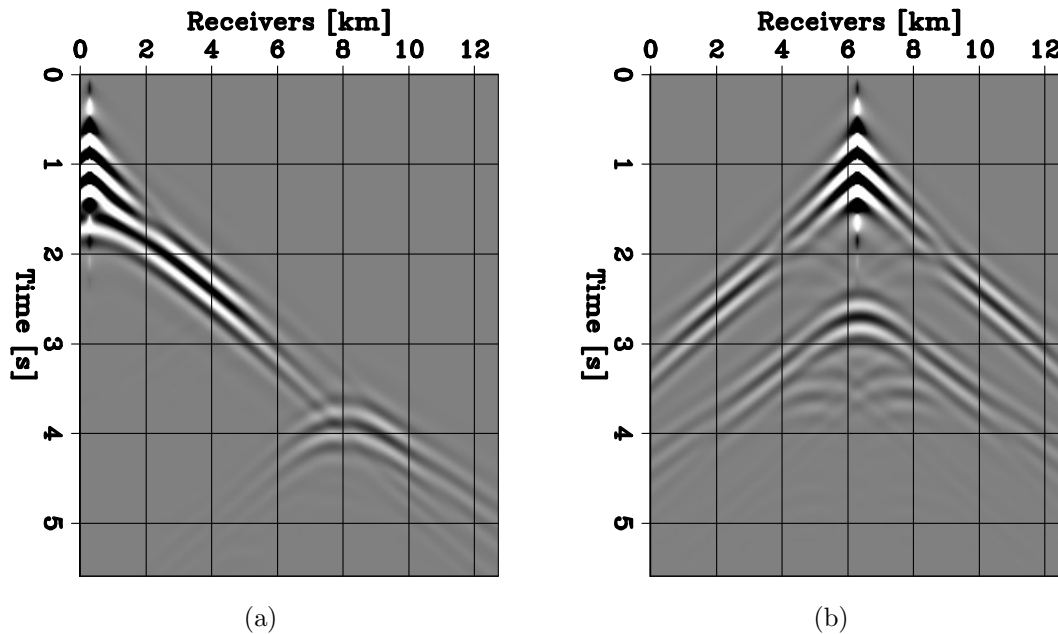


Figure 24: Two representative shot gathers generated by a seismic source containing energy only within the 1.5-6 Hz frequency range. (a) Source located at $x = 0.3$ km. (b) Source located at $x = 6.3$ km.

Understanding the events in the data

In order to better understand the origin and the wave path of each event present in the recorded shot gathers, we generate data (with the true model shown in Figure 21a) using a higher frequency seismic source containing energy as high as 30 Hz (we used a finite-difference sampling grid of 25 m for both directions). Figure 25a shows one shot gather for a source located at a horizontal position of $x = 6.35$ km. Figure 25b shows the same shot gather where the different events have been labeled with colored numbers. We can distinguish five distinct events in Figure 25b. Figures 26 shows twelve labeled snapshots of the wavefield that gave rise to the recorded shot gather in Figure 25b.

- The first event (event 0, white arrow in Figure 25b) displays a linear moveout and corresponds to the direct arrival of the incident wavefield (without any interaction with the interface between the two layers).
- Event 1 (blue arrows in Figures 25b and 26b) corresponds to the back-scattering of the incident wavefield as it interacts with the sharp corners on the edges of the synclinal basin. The corners act as diffracting points and the recorded event shows a hyperbolic moveout observable in the shot gather.
- Event 2 is generated when the incident wavefield reflects from the bottom of the basin. The wavefield later refocuses at the synclinal focal point (Figure 26d).

This “creates” a wavefield similar to the one that would have been generated by a virtual point source located at the focal point (red arrow in Figure 25b), which can be observed directly by examining the wavefield snapshots (Figures 26d-g).

- We believe event 3 (green arrows in Figure 25b) is generated by the overlapping of a reflection from the bottom of the synclinal basin with the “tails” of the incident scattered wavefield after its interaction with the sharp corners (event 1) (at this point, we cannot fully explain the mechanism that gives rise to this event). Nevertheless, this generates two up-going wavefields (event 3) observable in Figures 26f-k (blue arrows).
- Event 4 (purple arrows in Figure 25b) stems from the diffraction of both up-going wavefields (i.e., event 3) by the corners of the synclinal basin. Their respective wave path can be observed in Figures 26j-l.

Finally, Figures 27a-c shows the observed, predicted and residual data computed with the initial velocity model for a shot located at $x = 6.3$ km. Figure 27c clearly illustrates the overlapping of “true” and wrongly predicted events (i.e., the reflection of the incident background wavefield from the misplaced horizontal interface present in the initial model).

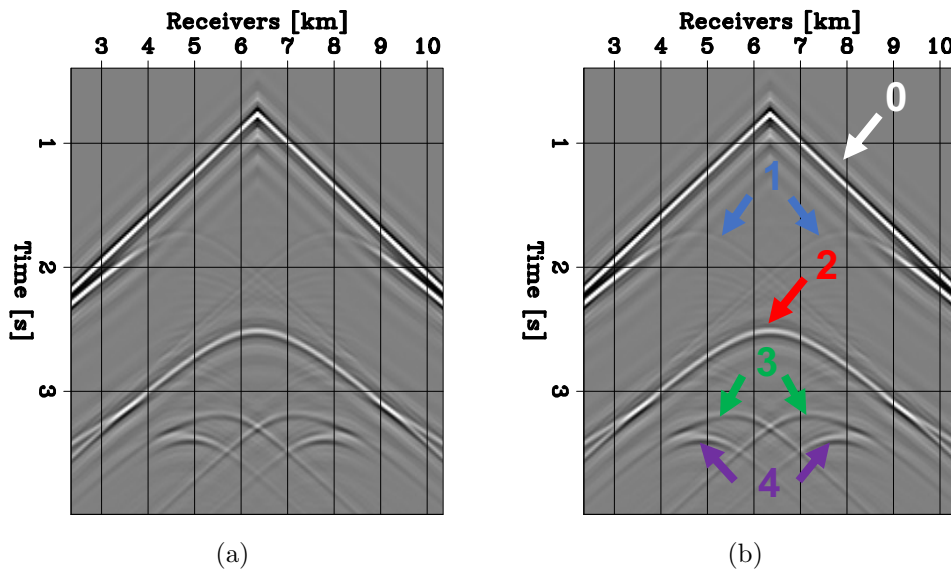


Figure 25: (a) Shot gather for a source located at $x = 6.35$ km containing energy within the 2-30 Hz frequency range. (b) Identical shot gather as (a) with labeled seismic events.

Conventional FWI

We first conduct a conventional FWI approach to illustrate its inability at recovering the true model. We invert the data generated by the seismic source containing energy

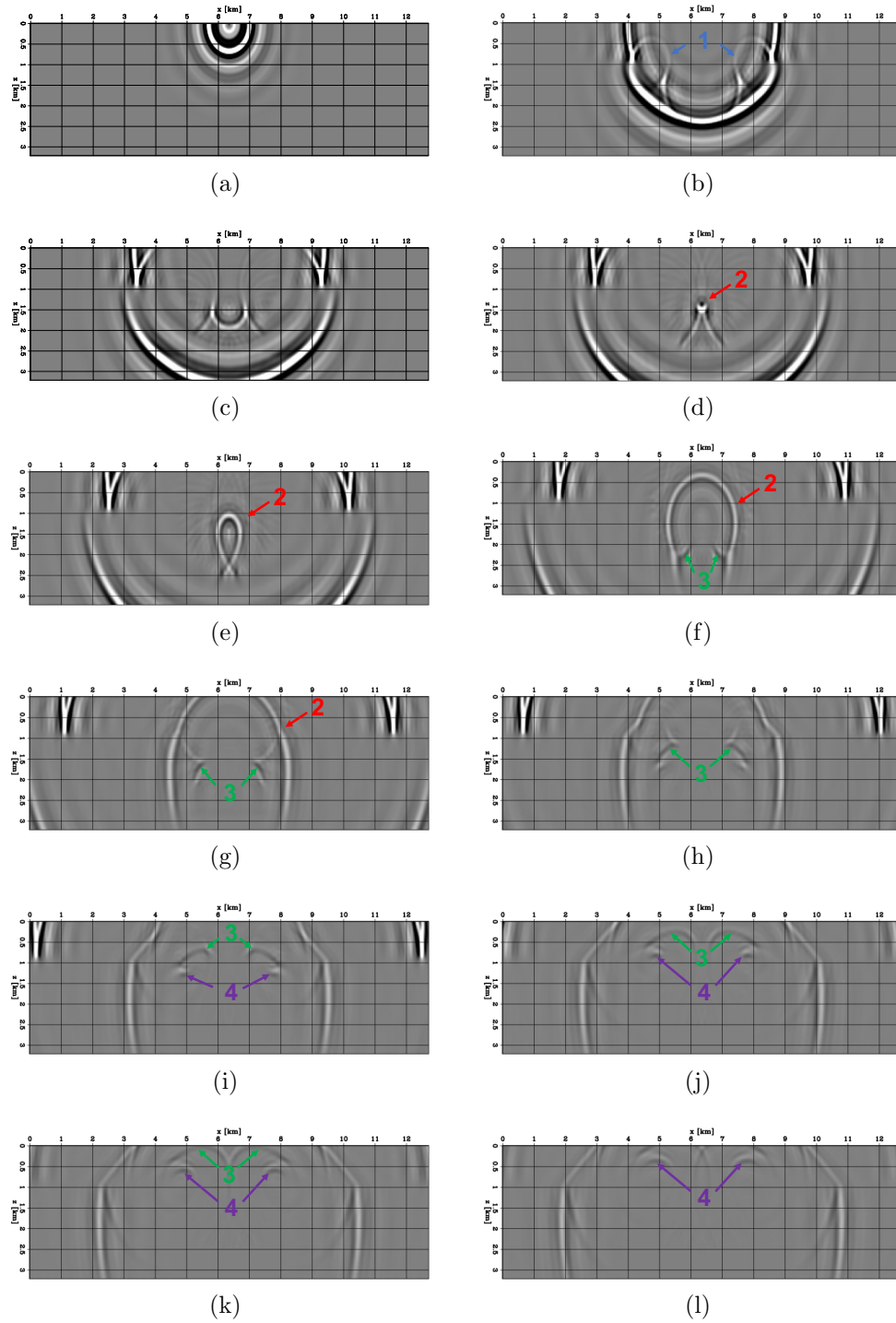


Figure 26: Wavefield snapshots generated by a source located at $x = 6.35$ km and containing energy within the 2-30 Hz frequency range. Each panel shows the wavefield at a given time step.

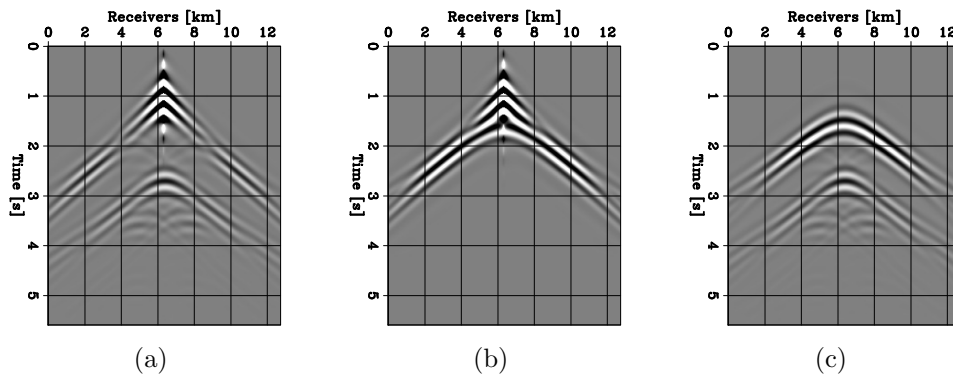


Figure 27: Shot gather for a source located at $x = 6.3$ km and containing energy within the 1.5-6 Hz frequency range. (a) Observed data. (b) Predicted data with the initial velocity model. (c) Initial data difference.

within the 1.5-6 Hz frequency range. Figure 28 shows the inverted model after 500 iterations of BFGS, which confirms that the FWI objective function has converged to a local minimum. Moreover, Figure 29b show the predicted data generated from the FWI inverted model, which is unable to accurately predict the triplications generated by the synclinal feature in the true model.

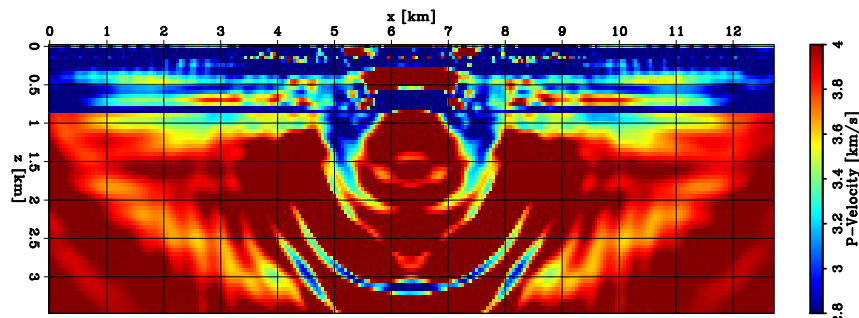


Figure 28: Inverted model using conventional FWI after 500 iterations of BFGS, and energy contained in the 1.5-6 Hz frequency range.

Model-space multi-scale FWIME

We apply FWIME by simultaneously inverting all data available in the 1.5-6 Hz frequency range (the same data used for the FWI workflow). We use two spline grids throughout our inversion scheme. The first spline grid has a sampling of 500 m in both the z - and x -directions. However, in the vicinity of the interface between the two layers, we use a spacing of 50 m in the z -direction in order to preserve the sharpness present in the initial model. The second spline grid is identical to the finite-difference grid.

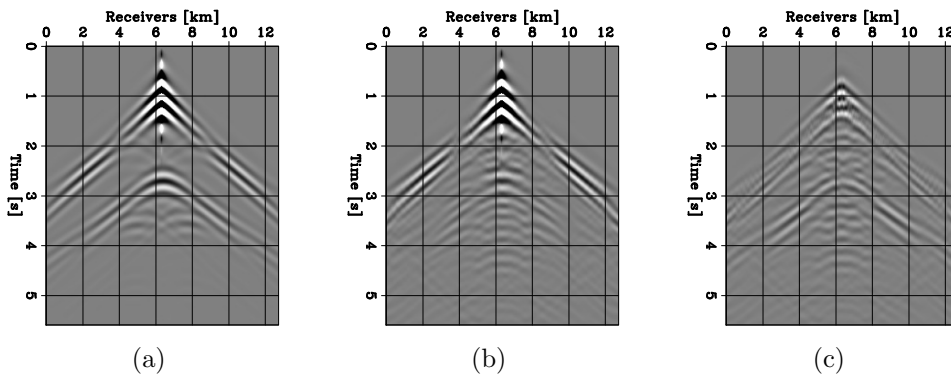


Figure 29: Shot gather at $x = 6.3$ km. (a) Observed data. (b) Predicted data with the inverted model using conventional FWI. (c) Data difference.

For this numerical experiment, we chose horizontal subsurface offsets as our extension type. Due to the large kinematic errors in the initial model, we employed 201 points of extension, providing us with horizontal subsurface offsets h_x ranging from -5 km to 5 km for $\tilde{\mathbf{p}}_{opt}^\epsilon$. Each variable projection step is conducted by minimizing objective function shown in equation 2 with 100 iterations of linear conjugate gradient.

Initial step

Figures 30a and b show two horizontal subsurface-offset domain common image gathers (SODCIGs) extracted from the initial extended optimal perturbation $\tilde{\mathbf{p}}_{opt}^\epsilon$ at $x = 4.0$ km and $x = 6.0$ km, respectively. The SODCIG located at $x = 4$ km contains weaker energy/events due to the fact that at that location, the initial model is already accurate. However, as we move closer to the basin, more energy is being back-projected into $\tilde{\mathbf{p}}_{opt}^\epsilon$. The kinematic error is so important that a maximum offset of approximately 4 km (on each side of the zero-subsurface axis) is needed to completely capture the energy (Figures 30b).

We chose $\epsilon = 1.0 \times 10^{-5}$ with the same (imperfect) strategy as for the Marmousi example. We also experimented different values (ranging from $\epsilon = 0.5 \times 10^{-5}$ to $\epsilon = 5.0 \times 10^{-5}$), which seemed to provide similar results. As mentioned in the Marmousi example, more tests need to be conducted to evaluate the robustness and the convergence efficiency of FWIME with respect to the ϵ -value.

Figure 31a shows the scaled Born component of the first search direction and Figure 31b displays the scaled tomographic component. Note that Figures 31a and b are not displayed on the same color scale. The Born component is approximately two orders of magnitude weaker than the tomographic component. Indeed, this is expected at early stages of the FWIME workflow where the inversion is primarily guided by the tomographic updates. Figure 31c shows the total search direction (i.e.,

the sum of the panels in Figures 31a and b), which is approximately identical to the tomographic component. Even though this search direction may seem promising (by comparing it to the “ideal” update in Figure 31c), its projection onto the first spline grid provides a much more interesting and accurate search direction (Figure 32a).

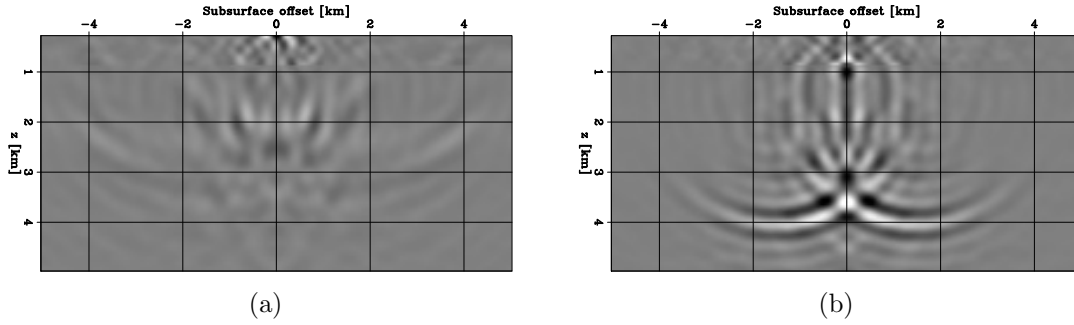


Figure 30: Horizontal subsurface offset domain common image gathers (SODCIGs) of the extended optimal perturbation $\tilde{\mathbf{p}}_{opt}^\epsilon$ computed at the initial step and extracted at two horizontal positions. (a) $x = 4.0$ km. (b) $x = 6.0$ km. Both figures are displayed on the same color scale.

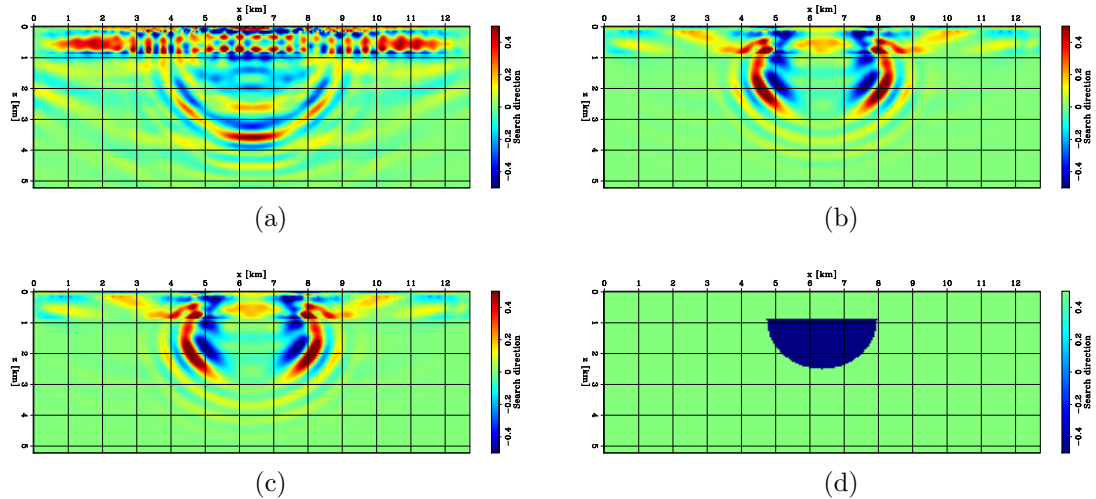


Figure 31: Scaled FWIME initial search directions on the finite-difference grid. (a) Born search direction. (b) Tomographic search direction. (c) Total search direction (sum of (a) and (b)). (d) True search direction. Note that (a) is displayed on a different color scale for clarity purpose. The amplitude of (a) is approximately two orders of magnitude smaller than the one of (b).

Inversion results

We conducted 28 iterations of our FWIME workflow on the first spline grid. As for the Marmousi example, the spline grid refinement was triggered when the solver could not

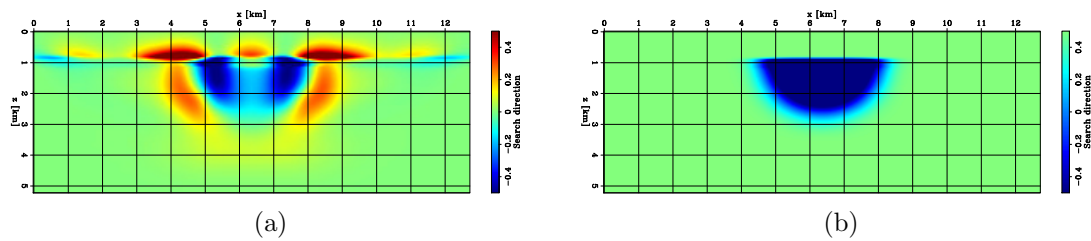


Figure 32: Initial scaled search directions after projection on the first spline grid. (a) FWIME first search direction. (b) True search direction.

find a proper step-length. The convergence curves for this grid is shown in Figure 33, and the inverted model is shown in Figure 35a. We used the inverted model on spline 1 as the initial model for the spline 2, and conducted 87 iterations of FWIME. For efficiency purposes, we did not wait until full convergence. The convergence curves and inverted model after inversion on spline 2 are shown in Figures 34 and 35b, respectively.

Finally, we used the FWIME inverted model as an initial model for conventional FWI. The inverted model after 200 iterations of BFGS is shown in Figure 35c. Figures 36 and 37 show vertical (and horizontal) velocity profiles of the initial, true and inverted models at various horizontal positions (and depths). The final result is quite accurate but still contains a weak reflector located at the initially wrongly positioned horizontal interface (at the top of the basin, at an approximate depth of $z = 0.8$ km). However, we think this artifact could potentially disappear if we were to conduct an inversion with higher frequency energy.

Figure 38 shows the evolution of the predicted data throughout various stages of our FWIME workflow (middle column). The inversion begins by generating the triplications in the wavefield (observable in Figure 38e) by first removing a portion of the incorrect high-velocity zone at the bottom of the basin (Figure 35a). After inversion on spline 2, most of the basin has been recovered, and the reflection from the initially mis-positioned horizontal interface (at $z \approx 0.8$ km) has been removed from the predicted data (Figure 38h). The last row shows the prediction after conducting conventional FWI using the FWIME inverted model as an initial guess. It enhances the accuracy of the results in both model-space (Figure 35c) and data-space (Figures 38k and l).

Spectral analysis

Figures 39 and 40 show the model updates and the amplitude spectrum of the model updates (at the different stages of the FWIME workflow), respectively. The inversion scheme begins by correctly updating the low-wavenumber components of the model in the z -direction (Figure 40a), but fails to update them in the x -direction. However, these missing features are gradually (but not perfectly) captured throughout the

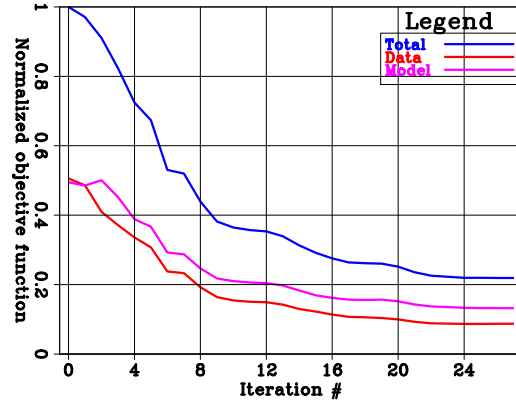


Figure 33: Scaled convergence curves of FWIME objective functions for the first spline grid.

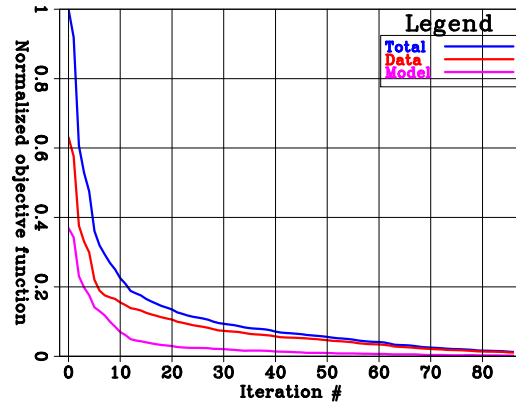


Figure 34: Scaled convergence curves of FWIME objective functions for the second (finite-difference) grid.

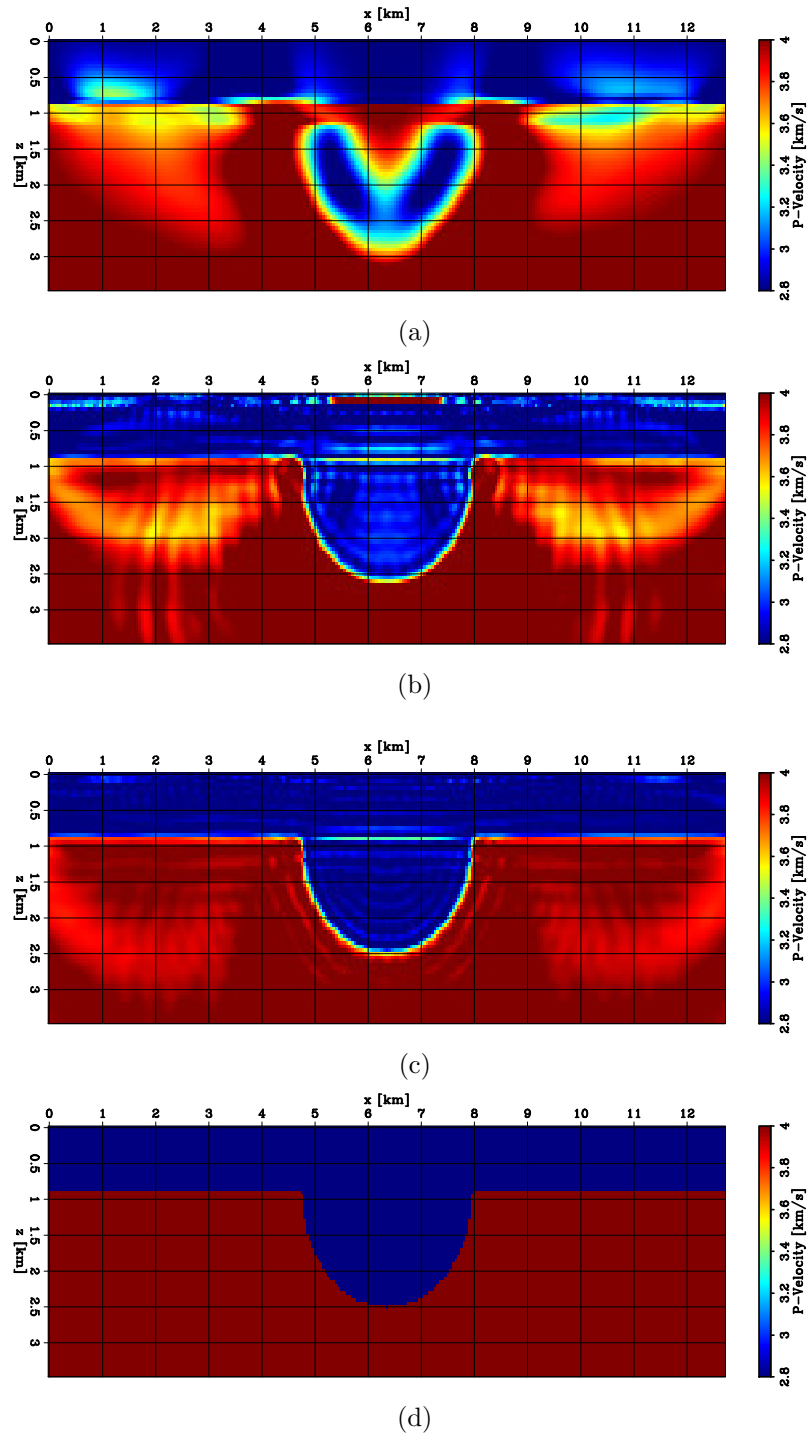


Figure 35: Inverted models at various stages of our FWIME workflow. (a) Inverted model after 28 iterations of FWIME on spline 1. (b) Inverted model after 87 iterations of FWIME on spline 2. (c) Inverted model after applying 200 iterations conventional data-space multi-scale FWI using (c) as an initial model. (d) True model.

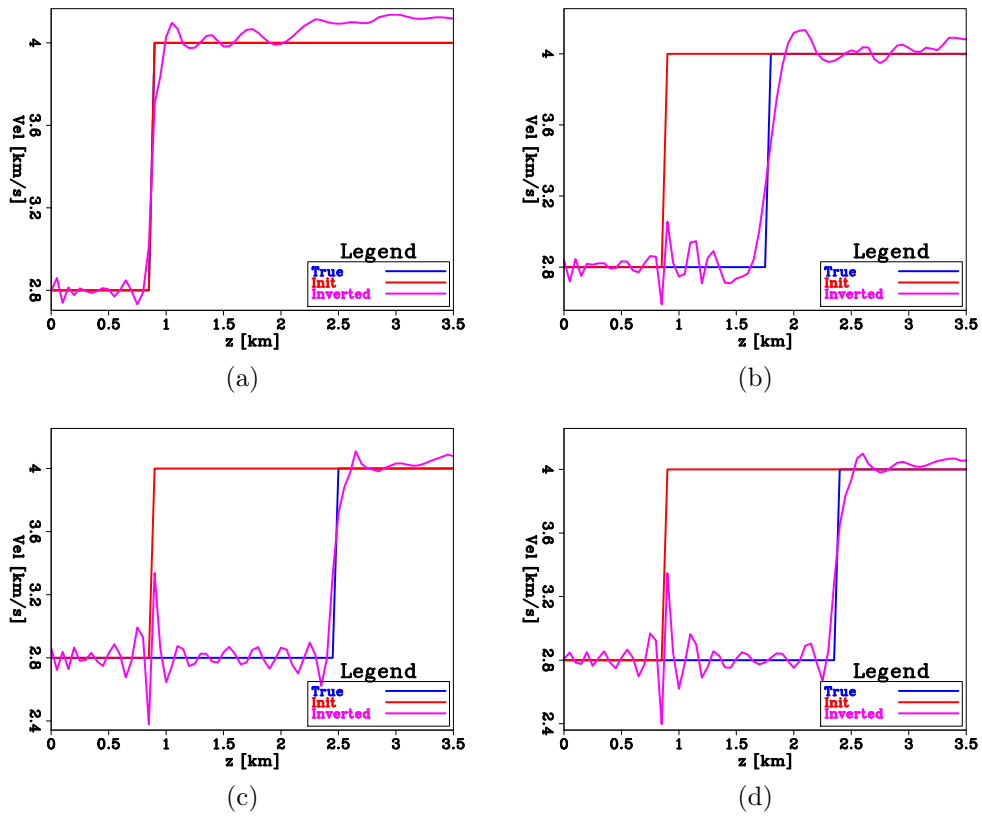


Figure 36: Vertical velocity profiles showing the initial model (red curve), the true model (blue curve), and the final FWIME inverted model (pink curve) extracted at four different depths. (a) $x = 4$ km, (b) $x = 5$ km, (c) $x = 6$ km, and (d) $x = 7$ km.

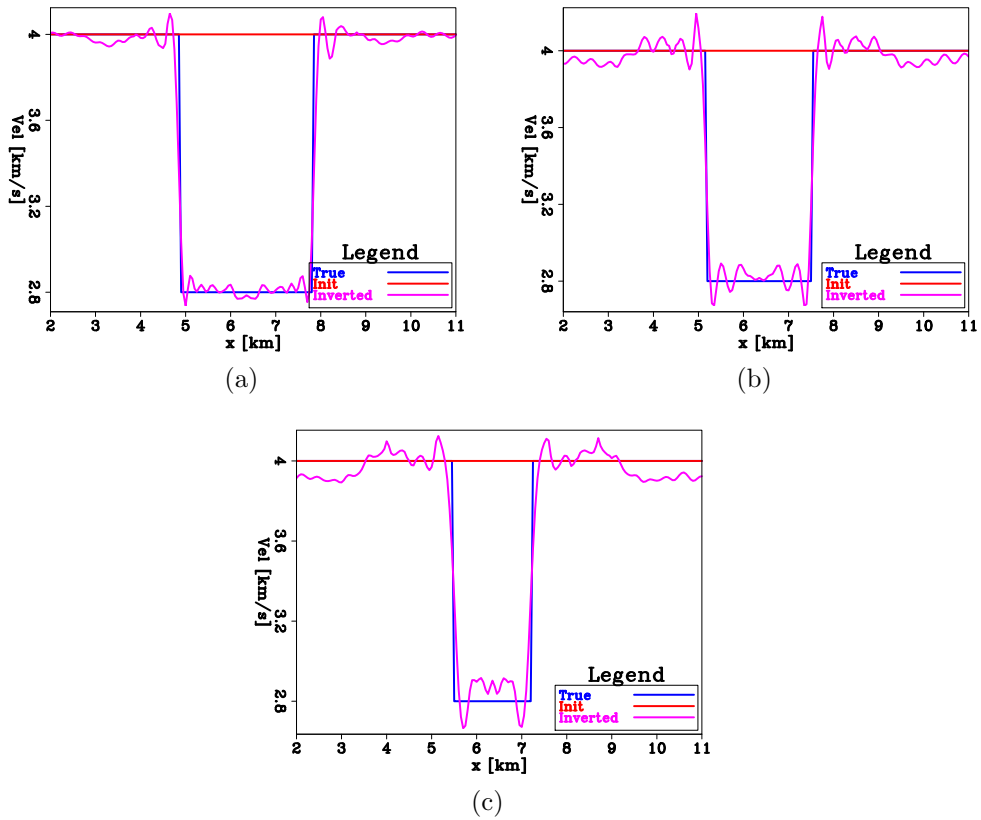


Figure 37: Horizontal velocity profiles showing the initial model (red curve), the true model (blue curve), and the final FWIME inverted model (pink curve) extracted at three different horizontal positions. (a) $z = 1.5$ km, (b) $z = 2.0$ km, and (c) $z = 2.25$ km.

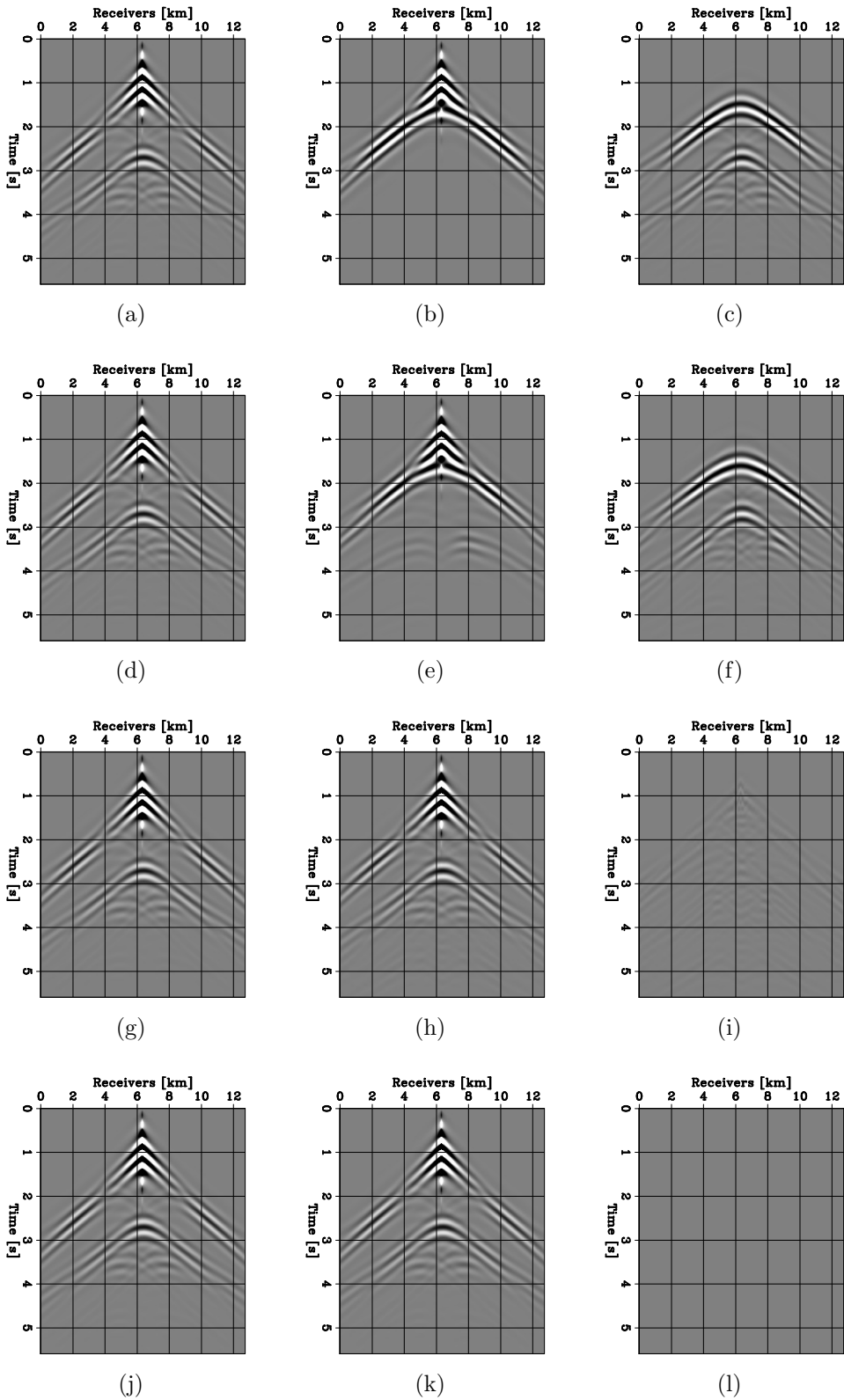


Figure 38: Observed data (left column), predicted data (middle column), and data difference (right column) for a shot located at $x = 6.3$ km at various stages of the FWIME workflow. First row was computed with initial model, second row with the FWIME inverted model after spline1, third row with spline 2, and fourth row with the final FWIME inverted model. *SEP-177*

remaining stages of the workflow (Figure 40b and c). In fact, we can see in Figures 39b and c that the vertical edges of the basin are better resolved and their sharpness is improved. Even though the inversion still misses some energy in that part of the spectrum (likely due to finite acquisition aperture), it has managed to recover an accurate model, which could potentially be improved by conducting this experiment by inverting higher frequency data.

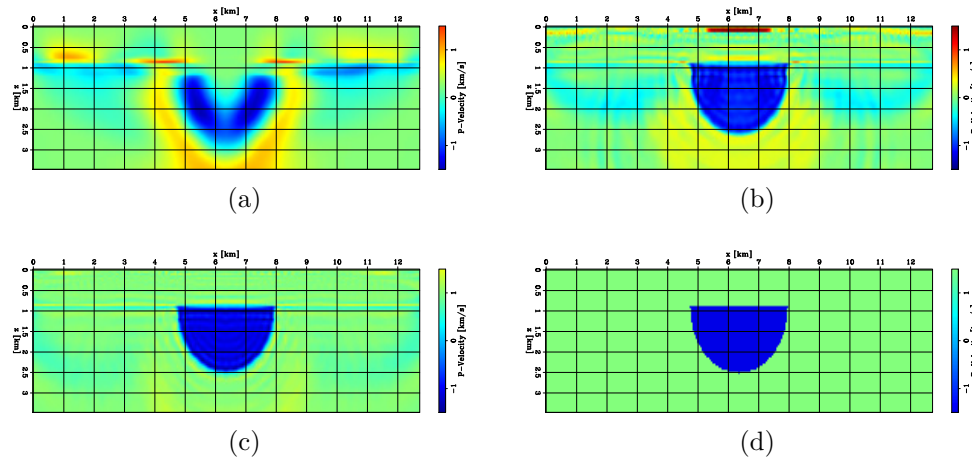


Figure 39: Velocity difference between inverted and initial models at difference stages of FWIME. (a) After inversion on spline 1. (b) After inversion on spline 2. (c) Final inverted model. (d) True model difference.

Imaging

For QC purposes, we migrate the observed data (to which we subtracted the direct arrival) using the initial velocity model (Figures 41a) and the final velocity model (Figures 41b). They show a clear improvement, which is confirmed by the angle-domain common images gathers (ADCIGs) extracted at various positions in Figure 42. We can see from the third and fourth columns in Figure 42 that the bottom of the basin (initially wrongly positioned) has been imaged quite accurately with a large improvement in the flatness of the ADCIGs.

Summary of the syncline model

We showed that our model-space multi-scale FWIME approach was able to perform well on this numerical example. First, it managed to handle the phase identification issue mentioned by the Seiscope team. Second, it was successful at removing a large area filled with incorrect velocity values (with strong velocity-contrast and sharp interfaces). We conducted conclusive quality checks to evaluate the quality of our results. Both accomplishments are quite promising as we are currently tackling imaging challenges in the presence of complex overburdens.

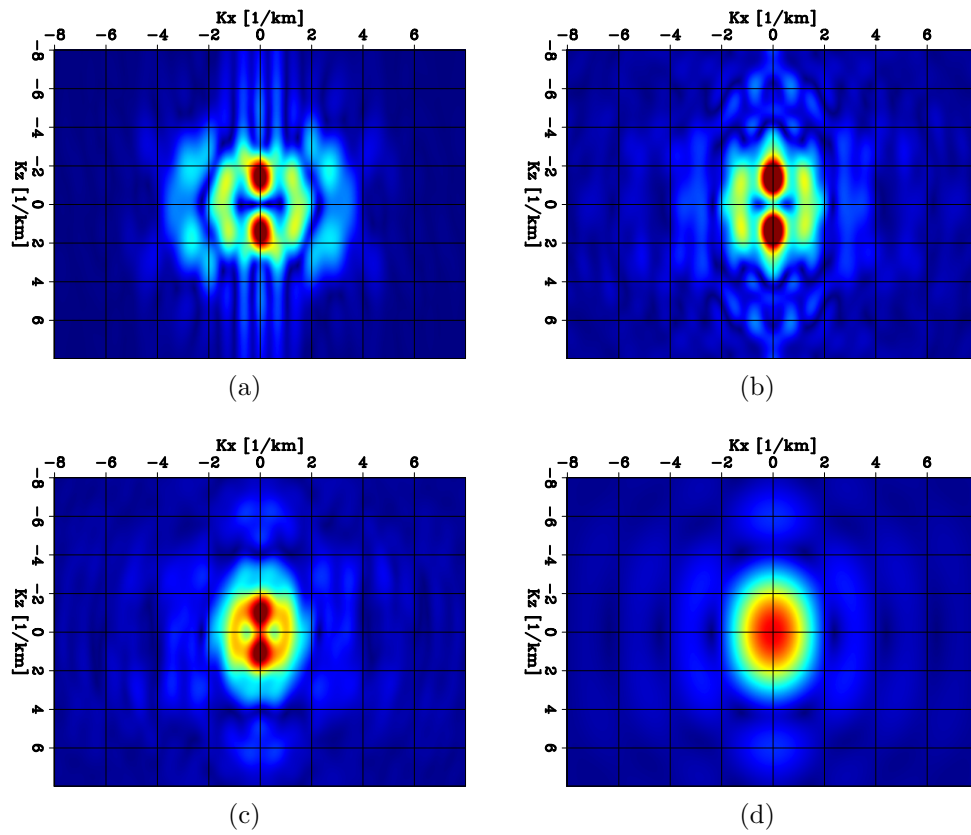
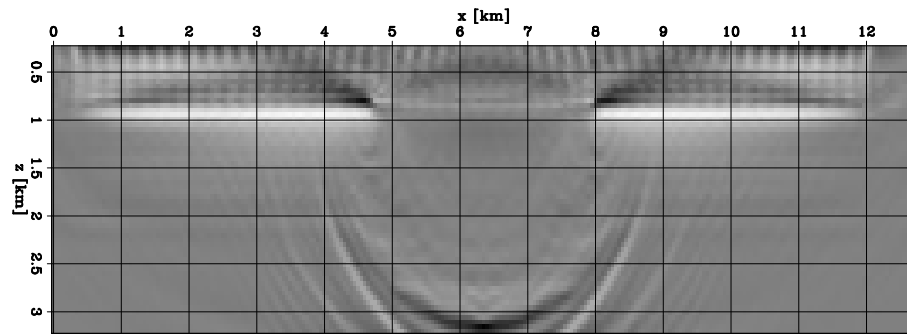
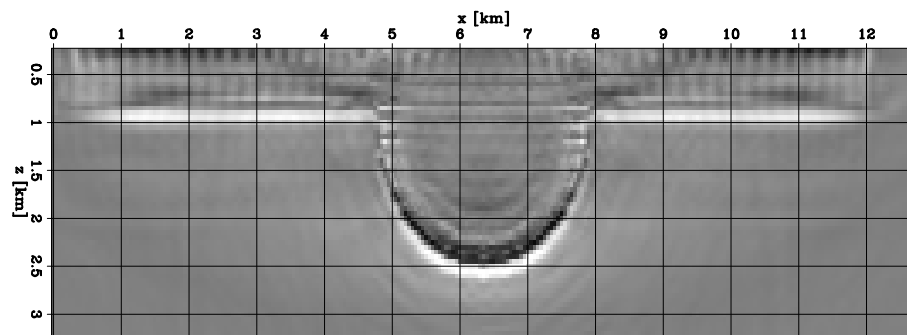


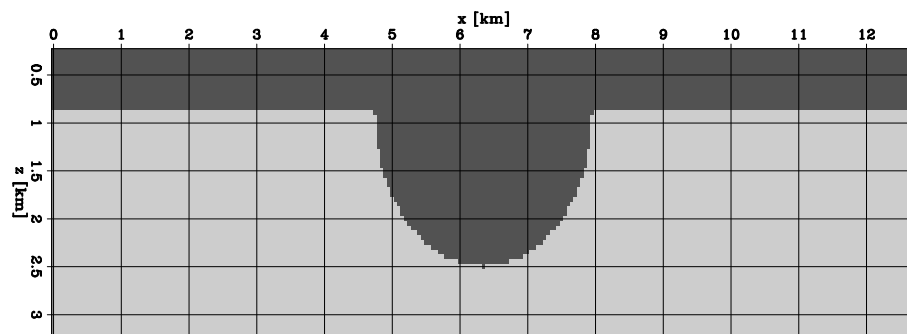
Figure 40: Amplitude spectrum (wavenumber domain) of model updates (i.e., amplitude spectrum of the Fourier transform of the difference between inverted and initial models) at different stages of our FWIME workflow. (a) After inversion on spline 1. (b) After inversion on spline 2. (3) Final inverted model. (d) True model difference.



(a)



(b)



(c)

Figure 41: Zero-offset migrated images computed with different velocity models. (a) Initial velocity model. (b) Final FWIME inverted model. (c) True velocity model (for reference).

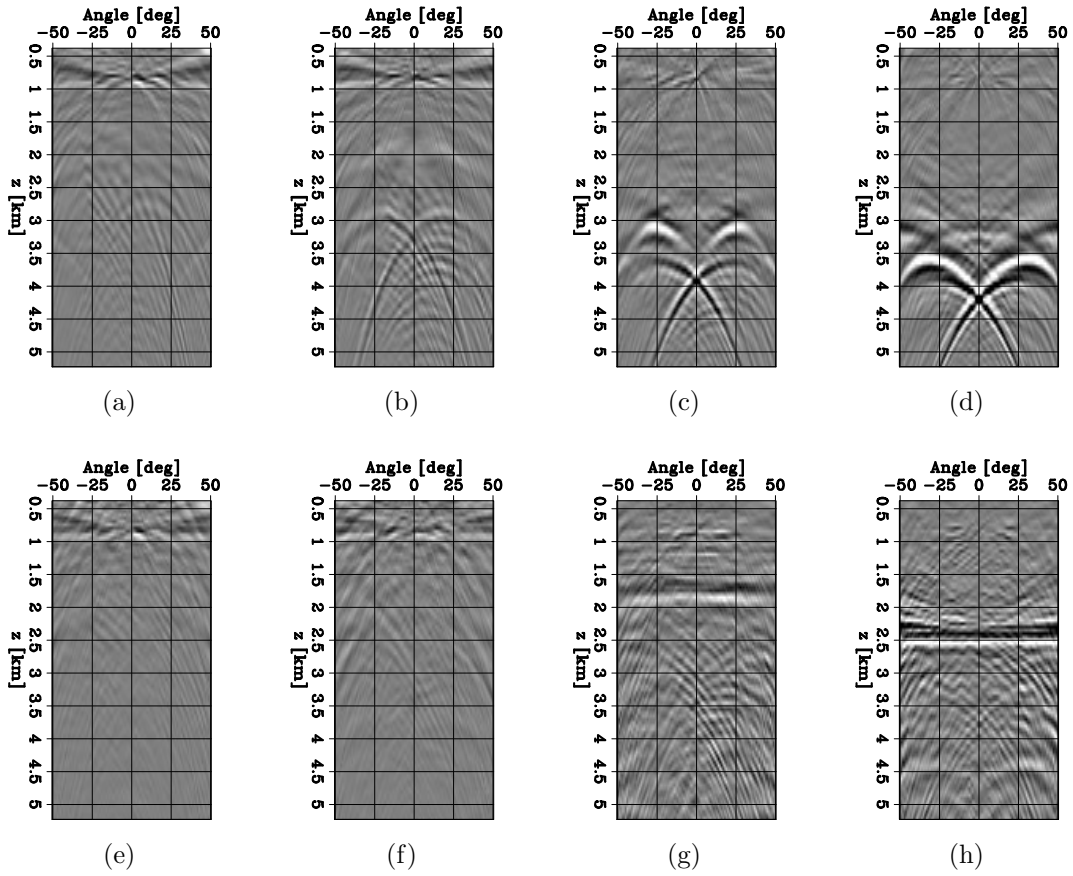


Figure 42: Angle domain common image gathers (ADCIGs) computed with the initial model (top row) and the FWIME inverted model (bottom row) at four different horizontal positions. First column is at $x = 3$ km, second column is at $x = 4$ km, third column is at $x = 5$, and fourth column is at $x = 6$ km.

CONCLUSIONS AND ROAD AHEAD

By conducting more experiments with FWIME, we were able to gain better insight on how to parametrize and calibrate the technique, thereby allowing us to produce a more robust and less user-intensive product. This also led to a great improvement of our results (compared to our previous report) on the standard Marmousi benchmark. Moreover, our conclusive results on the syncline model allows us to think that FWIME can potentially perform well in areas with very complex overburdens.

We want to stress the fact that the tests conducted in this report remain preliminary. Our goal was to first recover accurate, high-resolution results in a mathematically consistent and automatic manner. We wanted to understand our method in great depths in order to later improve its efficiency as we move to 3D field datasets.

Moving forward, we plan to work focus on three goals, (1) improving the efficiency of the method (as previously mentioned), (2) apply it in the presence of complex overburdens, and (3) test its ability to handle elastic effects.

ACKNOWLEDGEMENTS

We would like to thank the Seiscope consortium for allowing us to report our results on their synthetic “synclinal basin” velocity model. Moreover, we would like to personally thank Jean Virieux, William Symes, and Mark Meadows for their wise comments during our fruitful discussions, as well as all the interest they showed for our work. In many ways, they greatly contributed to make FWIME work. We also thank Paul Williamson for giving us the opportunity to collaborate with Total and test FWIME on a realistic subsalt imaging problem. Finally, Guillaume Barnier thanks BP Subsurface Technical Centre for allowing him to work on FWIME in 2017 when the technique was still at its very early stage.

REFERENCES

- Barnier, G. and E. Biondi, 2019, Full waveform inversion by model extension using a model-space multi-scale approach: SEP-Report, **176**, 11–30.
- Barnier, G., E. Biondi, and B. Biondi, 2018a, Full waveform inversion by mode extension: Presented at the SEG Technical Program Expanded Abstracts 2018, Society of Exploration Geophysicists.
- , 2018b, Full waveform inversion by model extension: SEP-Report, **172**, 153–171.
- Barnier, G., E. Biondi, and R. Clapp, 2019, Model-space multi-scale approach for waveform inversion using spline interpolation: SEP-Report, **176**, 1–10.
- Biondi, B. and A. Almomin, 2012, Tomographic full waveform inversion (TFWI) by combining full waveform inversion with wave-equation migration velocity analysis,

- in* SEG Technical Program Expanded Abstracts 2012, 1–5, Society of Exploration Geophysicists.
- , 2013, Tomographic full waveform inversion (TFWI) by extending the velocity model along the time-lag axis, *in* SEG Technical Program Expanded Abstracts 2013, 1031–1036, Society of Exploration Geophysicists.
- , 2014, Simultaneous inversion of full data bandwidth by tomographic full-waveform inversion: *Geophysics*, **79**, WA129–WA140.
- Biondi, E., R. G. Clapp, and G. Barnier, 2019, A flexible library for geophysical inverse problems – structure and usage: *SEP-Report*, **176**, 261–276.
- Fu, L. and W. W. Symes, 2017, A discrepancy-based penalty method for extended waveform inversion: *Geophysics*, **82**, R287–R298.
- Golub, G. H. and V. Pereyra, 1973, The differentiation of pseudo-inverses and nonlinear least squares problems whose variables separate: *SIAM Journal on numerical analysis*, **10**, 413–432.
- Huang, Y. and W. W. Symes, 2015, Born waveform inversion via variable projection and shot record model extension, *in* SEG Technical Program Expanded Abstracts 2015, 1326–1331, Society of Exploration Geophysicists.
- Martin, G. S., R. Wiley, and K. J. Marfurt, 2006, Marmousi2: An elastic upgrade for marmousi: *The Leading Edge*, **25**, 156–166.
- Rickett, J., 2013, The variable projection method for waveform inversion with an unknown source function: *Geophysical Prospecting*, **61**, 874–881.
- Symes, W. W. and M. Kern, 1994, Inversion of reflection seismograms by differential semblance analysis: Algorithm structure and synthetic examples: *Geophysical Prospecting*, **42**, 565–614.
- Virieux, J. and S. Operto, 2009, An overview of full-waveform inversion in exploration geophysics: *Geophysics*, **74**, WCC1–WCC26.